Evaluating the CoMorph-A parameterization using idealised simulations of the two-way coupling between convection and large-scale dynamics

Received: 13 October 2022 | Revised: 2 May 2023 | Accepted: 16 June 2023

DOI: 10.1002/qj.4547

Quarterly Journal of the Royal Meteorological Society RMetS

RESEARCH ARTICLE

Evaluating the CoMorph-A parametrization using idealized simulations of the two-way coupling between convection and large-scale dynamics

Chimene L. Daleu[1] | **Robert S. Plant**[1] | **Alison J. Stirling**[2] | **Mike Whitall**[2]

[1]Department of Meteorology, University of Reading, Reading, UK

[2]Met Office, Exeter, UK

Correspondence
Chimene L. Daleu, Department of Meteorology, University of Reading, Reading, RG6 6ET, UK.
Email: c.daleu@reading.ac.uk

Funding information
Natural Environment Research Council, Grant/Award Number: NE/N013743/1

Abstract

We present a new methodology to test the interactions of convection schemes with their larger scale environment. A single-column model (SCM) using the new Met Office convection scheme, CoMorph-A, and the new Met Office–Natural Environment Research Council cloud-resolving model (CRM) are coupled to damped-gravity-wave-derived large-scale dynamics. The coupled models are used to investigate convective responses to stimulus forcings under the influence of interactive large-scale dynamics. Within CoMorph-A, the default entrainment varies with the prediction of convection size that is dependent on earlier rainfall, and the sensitivity of the SCM results to the entrainment formulation is explored. We demonstrate that the behaviour of the SCM using CoMorph-A is now very similar to that of the CRM. For temperature or moisture stimulus applied separately, the SCM adjusts to a new equilibrium that is similar to that in the CRM, but its transient convective responses to stimuli acting to suppress convection are markedly too fast. For a combination of stimuli acting to enhance convection, the SCM responses are stronger than in the CRM. Finally, convective rainfall in the SCM is relatively insensitive to a combination of stimuli acting to enhance and suppress convection simultaneously, in agreement with the CRM. However, the SCM recovery from a non-precipitating state is overly delayed for the default entrainment formulation but is too rapid when the entrainment rate is fixed at a low rate to represent only the deep convective state. We examined the responses to moisture stimuli of different strengths. Both models produce a monotonic increase of precipitation with column relative humidity (CRH) as well as the sharp increase of precipitation as CRH exceeds a threshold, as seen in observations. Though both models correctly capture the observed CRH threshold, differences from the observed precipitation–CRH relationship are noted. For instance, above the threshold the increase of precipitation with CRH is more abrupt in the SCM than in the CRM and observations. A similar behaviour is obtained in the SCM using low entrainment rate.

KEYWORDS

cloud-resolving models, convection–large-scale environment interaction, convective parametrization

1 | INTRODUCTION

The representation of moist convection remains the major source of uncertainty in current state-of-the-art general circulation models (GCMs). The heating from convection is the most important source of energy driving the large-scale atmospheric flow, and the large-scale flow in turns provides a forcing for convection. This two-way interaction between convection and large-scale circulation regulates the global climate, and our understanding of it stands to lead to improvements in the representations of convection in numerical models used for weather forecast and climate prediction.

Because of the large range of spatial scales involved between individual convective clouds and the large-scale flow, relatively few studies have explicitly simulated both processes due to computational cost (e.g., Liu *et al.*, 2009; Holloway *et al.*, 2012; Ferrett *et al.*, 2021; Hertwig *et al.*, 2021; Haslebacher *et al.*, 2022). To keep the computational cost manageable, most studies have used GCMs with parametrized convection (e.g., Randall *et al.*, 2007; Lin *et al.*, 2008; Endris *et al.*, 2021; Muetzelfeldt *et al.*, 2021). Since a single-column model (SCM) version of a GCM is computationally cheap to run, it is often used to evaluate how parametrized physics would perform as a separate component of the parent GCM (Randall *et al.*, 1996). The performance of SCM parametrized physics is often evaluated by comparing results with observations or with results from cloud-resolving models (CRMs) or large-eddy models (e.g., Iacobellis and Somerville, 1991; Xu and Arakawa, 1992; Xu, 1994; Lee *et al.*, 1997; Xie *et al.*, 2002; Xu *et al.*, 2002, 2005; Daleu *et al.*, 2015; Daleu *et al.*, 2016; Daleu *et al.*, 2017). Such comparisons have proven to be useful to inform parametrization development (e.g., Siebesma and Cuijpers, 1995; Bretherton *et al.*, 2004; Rio *et al.*, 2010). Here, we conduct such SCM–CRM comparisons to evaluate the performance of the new Met Office convective parametrization scheme (CoMorph-A) and facilitate its improvement.

In recent years, CRMs and SCMs modified to implement large-scale parametrization methods have been exploited to study the two-way interaction between convection and large-scale circulation, without explicitly simulating the large scale. There are various forms of parametrized large-scale methods that were developed based on physical understanding of the tropical atmosphere. These include the weak-temperature gradient (WTG) or spectral WTG (e.g., Sobel and Bretherton, 2000; Raymond, 2007; Sessions *et al.*, 2010; Daleu *et al.*, 2012; Herman and Raymond, 2014), damped gravity wave (DGW; e.g., Kuang, 2008; Kuang, 2011; Wang *et al.*, 2013; Edman and Romps, 2014), and quasi–geostrophic (QG; e.g., Nie and Sobel, 2016) approximations.

Several modelling studies have explored the impacts of moisture perturbations on explicitly resolved convection (e.g., Lucas *et al.*, 2000; James and Markowski, 2010; Kuang, 2010; Tulich and Mapes, 2010; Wang and Sobel, 2012) or parametrized convection (e.g., Sobel and Bellon, 2009) interacting with a parametrized large-scale circulation. Wang and Sobel (2012) in their CRM study found that upper tropospheric drying had almost no effect on deep convection, whereas drying imposed in the lower or middle troposphere was effective in reducing rain rate, more strongly so for lower tropospheric drying. A similar sensitivity to moisture perturbations was obtained in other coupled CRM studies (e.g., Kuang, 2010; Tulich and Mapes, 2010). In contrast to CRM results, the study of Sobel and Bellon (2009) using two different SCMs revealed that drying imposed in the middle troposphere was more effective in suppressing deep convection than when imposed in the lower troposphere.

Other studies have used SCMs and/or CRMs coupled to a parametrized large-scale circulation to examine convective responses to perturbations of temperature and moisture fields (e.g., Mapes, 2004; Raymond and Sessions, 2007; Herman and Raymond, 2014; Sessions *et al.*, 2015). Using a CRM, Mapes (2004) found that perturbations to moisture and temperature corresponding to a second baroclinic vertical displacement mode were more effective in enhancing the transient response in rainfall compared with perturbations corresponding to a first baroclinic vertical displacement mode. The CRM study of Sessions *et al.* (2015) revealed that changing the environmental atmospheric stability, enforced by warming (or cooling) above 5 km and cooling (or warming) below, has a drastic impact on the shape of the vertical motion – and thus the character of convection, while increasing (or reducing) the environmental moisture generates more (or less) intense convective rainfall without qualitatively changing the shape of the large-scale motion. Similar responses of convection to changes in environmental atmospheric stability and moisture were obtained in the CRM studies of Raymond and Sessions (2007); Herman and Raymond (2014). However, they contrast with the CRM study of Wang and Sobel (2012), who showed that lower tropospheric drying reduces top-heaviness of convection and can completely shut off deep convection if stronger drying is applied.

In these previous studies, perturbations were introduced by imposing continuous drying to the simulated region (e.g., Sobel and Bellon, 2009; Wang and Sobel, 2012) or by imposing anomalies to the thermodynamic fields of the simulated region (e.g., Mapes, 2004) or of the reference column representing the large-scale environment surrounding the simulated region (e.g., Raymond and Sessions, 2007; Herman and Raymond, 2014; Sessions

et al., 2015). Here, we have imposed idealized perturbations to temperature and/or moisture tendency profiles of the simulated region. This is equivalent to enforcing changes in moisture and atmospheric stability of the simulated column as done in the study of Mapes (2004) and opposed to other studies that enforced changes in moisture and atmospheric stability of a reference column (e.g., Raymond and Sessions, 2007; Herman and Raymond, 2014; Sessions *et al.*, 2015). In contrast to Mapes (2004), who introduced perturbations over the first 10 min of 12-hr simulations, we have imposed perturbations continuously throughout the simulations. We followed the CRM study of Sessions *et al.* (2015) and explored the full range of possible combinations of perturbations. Finally, we explored convective responses to a range of drying and moistening rates. This follows the study of Derbyshire *et al.* (2004), who explored the sensitivity of convection to environmental moisture. However, in contrast to this study, in which the parametrized large-scale circulation advects heat and moisture vertically within the domain and advects moisture horizontally according to mass continuity, Derbyshire *et al.* (2004) represented large-scale dynamics via nudging of the simulated thermodynamic and horizontal wind profiles to prescribed target profiles with a nudging time-scale of 1 hr. As this study mainly focuses on evaluating CoMorph-A, we will perform simulations with temperature and/or moisture tendency perturbations using a CRM as a reference and using the SCM with the CoMorph convection scheme. We will demonstrate that comparing SCM simulations against equivalent CRM simulations is a useful technique to evaluate the ability of the parametrized physics to reproduce an appropriate convective response in the presence of coupling to large-scale circulations.

2 | MODEL DESCRIPTION

2.1 | The new Met Office–Natural Environment Research Council cloud model: MONC

The Met Office–Natural Environment Research Council (NERC) cloud model (MONC; (Brown *et al.*, 2020) is a rewrite of the original Met Office large-eddy model to improve computational efficiency. It has been successfully used to study cloud microphysics (e.g., Dearden *et al.*, 2018), boundary-layer turbulence (Kealy *et al.*, 2019), and the diurnal cycle of deep convection (Daleu *et al.*, 2020).

All MONC simulations are performed using a three-dimensional domain of $128 \times 128 \times 20\,\text{km}^3$ with bi-periodic lateral boundary conditions and a Newtonian damping layer above 16 km (≈100 hPa) to absorb vertically propagating waves. This domain is big enough to accommodate an ensemble of convective clouds together with the compensating subsidence motions. At the same time, it is small enough to prevent self-aggregation of convection (Muller and Held, 2012), and so avoids the formation of circulations that may develop within the domain and favour mesoscale organization of convection (Bretherton and Smolarkiewicz, 1989; Tompkins, 2000). The horizontal grid spacing is 1 km, and there are 83 levels in the vertical, on a stretched grid with finer resolution near the surface. This relatively coarse resolution and small domain are pragmatic choices to keep computational demands manageable, because the total duration of the simulations is around 150 days.

Subgrid turbulent eddy fluxes are calculated using the three-dimensional Smagorinsky scheme. Cloud processes are represented using the newly developed Cloud AeroSol Interactive Microphysics (CASIM). CASIM has been successfully exploited in a variety of studies (e.g., Shipway and Hill, 2012; Hill *et al.*, 2015; Grosvenor *et al.*, 2017; Dearden *et al.*, 2018; McCoy *et al.*, 2018; Miltenberger *et al.*, 2018; Stevens *et al.*, 2018; Daleu *et al.*, 2020). CASIM is a user-configurable and multi-moment scheme that represents cloud water, rain, ice, snow, and graupel. In this study, each of those hydrometeor species is represented using prognostic variables for both the mixing ratios and number concentrations.

2.2 | Single-column model

We use the single column form of the Global Atmosphere GA8 configuration of the Met Office Unified Model. The GA8 configuration (not yet published) evolves from GA7 (Walters *et al.*, 2019) with some additional science changes. The domain has 85 levels in the vertical on a stretched grid extending from the surface to the model top at 20 km. Large-scale clouds are represented using the prognostic PC2 scheme of Wilson *et al.* (2008), and the associated microphysics parametrization is based on Wilson and Ballard (1999). The boundary-layer parametrization is that of Lock *et al.* (2000), and convection is represented using CoMorph-A – the new diagnostic mass flux convection parametrization under development at the Met Office (Whitall *et al.*, in preparation). In CoMorph-A, the traditional mass flux framework used in the existing convection scheme (Gregory and Rowntree, 1990) is generalized and extended. A description of the differences between CoMorph-A and the existing scheme is provided in the Appendix. One of the primary differences is the unified approach, in which separate schemes for "shallow", "congestus", and "deep" convection are

combined within a single scheme by adaptively varying the entrainment rate.

In CoMorph-A, the entrainment rate E is assumed to be inversely proportional to a "parcel radius" R:

$$E = M\frac{0.2}{R}. \tag{1}$$

The initial radius R_{init} at each height is proportional to the turbulent diffusivity K_{m} and inversely proportional to the turbulent vertical velocity variance $\overline{w'^2}$:

$$R_{\text{init}} = 8\alpha\frac{K_{\text{m}}}{\sqrt{\overline{w'^2}}}; \tag{2}$$

and the radius R of the combined parcel as it rises is a weighted average of the initation values, modified by the effects of entrainment – see Equation (A.6) in the Appendix. The dimensionless scaling factor α is optionally set as a linear function of the grid-mean surface precipitation rate (Pr) from the previous time step to allow the scheme to crudely represent increased organization of the convection by precipitation-driven cold pools, which promote larger scale updraughts with lower entrainment rates:

$$\alpha = \alpha_0 + MIN\left(\frac{\text{Pr}}{\text{Pr}_{\text{max}}}\frac{q_{\text{ref}}}{q_{\text{v}}}, 1\right)(\alpha_{\text{max}} - \alpha_0). \tag{3}$$

The values of Pr_{max}, q_{ref}, α_0, and α_{max} are given in the Appendix. This linear ramp function, Equation (3), allows CoMorph-A to smoothly transition from simulating non-precipitating shallow cumulus with small size (high E) through to heavily precipitating deep convection with large size (low E), for a given turbulence length scale in the triggering layers. The linear ramp function may be disabled by setting α to its maximum value, α_{max}. This forces CoMorph-A to use a low entrainment rate consistent with organized precipitating deep convection. Two types of SCM simulations are performed with the CoMorph-A convection scheme: the first uses the original version of CoMorph-A, which has the precipitation-dependent ramp switched on (variable E), and the second type disables the ramp function and sets the entrainment rate to represent deep convection (low E).

2.3 | Overall approach

For both models, the top (at 20 km ≈ 50 hPa) and bottom of the domain are rigid lids and the lower boundary is an ocean surface with a prescribed spatially homogeneous and time-independent sea-surface temperature of 28°C. No Coriolis force is applied, and the zonal-mean and meridional-mean wind components are relaxed toward vertically uniform values of $5\,\text{m}\cdot\text{s}^{-1}$ and $0\,\text{m}\cdot\text{s}^{-1}$ respectively, both with relaxation time-scale of 3 hr. Imposing a vertically uniform wind increases the value of surface evaporation (compared with the no-wind value) without affecting the dynamics of convection. The integration time step varies between 1 and 2 s in MONC, and it has a constant value of 5 min in all SCM simulations.

The particular interest of this study is to assess the impact of changes in moisture and/or atmospheric stability on convective development. Thus, for simplicity, we forced the models using a horizontally uniform and non-interactive cooling through the troposphere to prevent feedback that could arise from cloud–radiation interactions. Such idealized cooling, which roughly approximates the effects of outgoing long-wave radiation on the tropical troposphere, will be referred to as radiative cooling (or background forcing) and it is applied to temperature. It has a constant value of $1.5\,\text{K}\cdot\text{day}^{-1}$ from the surface up to 12 km and decreases linearly with height to reach $0\,\text{K}\cdot\text{day}^{-1}$ near 16 km.

3 | PARAMETRIZATION OF THE LARGE-SCALE DYNAMICS AND EXPERIMENTAL DESIGN

3.1 | Parametrization of the large-scale dynamics

Under the DGW mode, the large-scale circulation is derived from a combination of the momentum and thermodynamic equations. A second-order derivative of the large-scale pressure velocity $\overline{\omega}$ is related to the deviation of the domain-mean virtual temperature $\overline{T}_{\text{v}}$ from that of a predefined reference state $\overline{T}_{\text{v}}^{\text{Ref}}$; that is:

$$\frac{\partial}{\partial p}\left(\epsilon\frac{\partial\overline{\omega}}{\partial p}\right) = \frac{\kappa^2 R_{\text{d}}}{\overline{P}^{\text{Ref}}}\left(\overline{T}_{\text{v}} - \overline{T}_{\text{v}}^{\text{Ref}}\right), \tag{4}$$

where R_{d} is the gas constant of dry air. We fixed the mechanical damping coefficient $\epsilon = 1\,\text{day}^{-1}$ and solve the wave equation, Equation(4), with a single horizontal wave number $\kappa = 10^{-6}\,\text{m}^{-1}$. These are typical values used in other DGW studies (e.g., Wang and Sobel, 2011; Wang *et al.*, 2013; Daleu *et al.*, 2015; Daleu *et al.*, 2016).

The prognostic equations of potential temperature θ and water vapour q are modified to include the source or sink terms induced by $\overline{\omega}$; that is:

$$\frac{\partial\theta}{\partial t} = \cdots - \overline{\omega}\frac{\partial\overline{\theta}}{\partial p} \tag{5}$$

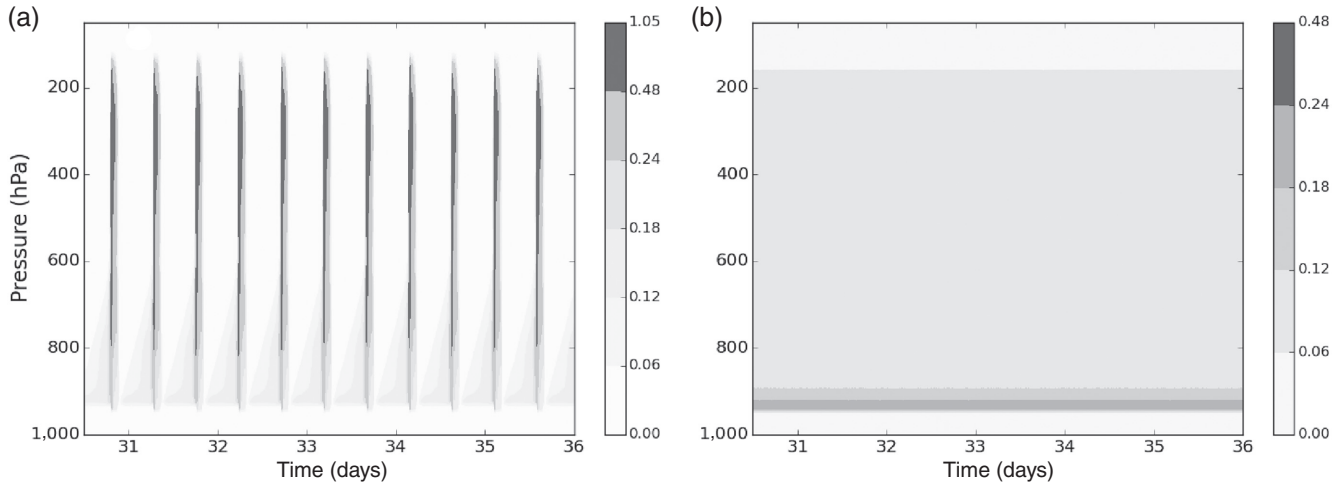

FIGURE 1 Time–height cross-sections of updraught mass flux ($Pa \cdot s^{-1}$). Results are the 15 min running mean obtained in the radiative–convective equilibrium simulations performed with the single-column model using (a) variable E or (b) low E.

and

$$\frac{\partial q}{\partial t} = \cdots - \overline{\omega}\frac{\partial \overline{q}}{\partial p} + \max\left(\frac{\partial \overline{\omega}}{\partial p}, 0\right)\left(\overline{q}^{\mathrm{Ref}} - \overline{q}\right). \qquad (6)$$

The term on the right-hand side of Equation (5) represents adiabatic cooling or warming. The first and second terms on the right-hand side of Equation (6) respectively represent the vertical and horizontal advection of water vapour. Note that the latter is non-zero only if there is convergence into the simulated column, and thus represents explicit "lateral entrainment" of the reference column air into the simulated domain (Raymond and Zeng, 2005). Such source or sink terms represent the net effects of the large-scale circulation on convection, and they have been used to generate convection with intensity and vertical structure similar to observations (e.g., Grabowski *et al.*, 1996). Full details of the implementation of our DGW method are given in Daleu *et al.* (2015); Daleu *et al.* (2016).

3.2 | Defining the reference state

Each model is run in radiative–convective equilibrium (RCE; DGW switched off) until a quasi-steady state is achieved in which the net convective heating balances the net radiative cooling. Figure 1 presents time–height cross-sections of updraught mass flux ($\rho g w$) obtained in the SCM. When using variable E, the SCM oscillates between states with suppressed (generating little or no precipitation) and heavily precipitating deep convection, in a manner not observed in MONC. This is likely because the equilibrium state requires representation of more than one cloud-radius type within the grid box. Though MONC allows a range of different updraught sizes to coexist simultaneously in different parts of the domain, the current configuration of CoMorph-A can only represent a single updraught type at a time, meaning that it cannot achieve an equilibrium state within an SCM framework on a given time step. Furthermore, the inclusion of a radius ramp that contains no intrinsic time-scale allows the scheme to oscillate rapidly between the different entrainment states. In contrast, limiting the scheme to access only low E allows the SCM simulations to attain an equilibrium state on each time step by producing continuous precipitating deep convection. Despite the fact that significant time variations occur when using variable E, the mean convective characteristics (averaged over a long period of integration) are close to those obtained in the SCM using low E. The RCE precipitation and evaporation rates are both 4.22 $mm \cdot day^{-1}$ for MONC and 4.32 $mm \cdot day^{-1}$ (or 4.27 $mm \cdot day^{-1}$) for the SCM using variable (or low) E, and the resulting profiles of θ, q, relative humidity (RH), and updraught mass flux are shown in Figure 2. For MONC, the mass flux is shown for all cloudy updraughts (grid points with mixing ratio of liquid cloud or ice greater than 10^{-5} $kg \cdot kg^{-1}$ and positive vertical velocity).

The shapes of the thermodynamic profiles are roughly similar, and the inter-model differences are within the range of differences obtained in other similar studies (e.g., Herman and Kuang, 2013; Daleu *et al.*, 2015; Hwong *et al.*, 2021). MONC has a lower column RH (CRH; calculated as the ratio of column-integrated water vapour to its saturation value) because its free troposphere is generally drier than that of the SCM. Although MONC has lower CRH and generates less deep convection, it is warmer and moister below 850 hPa, leading to more active precipitating shallow and congestus modes than are able to be

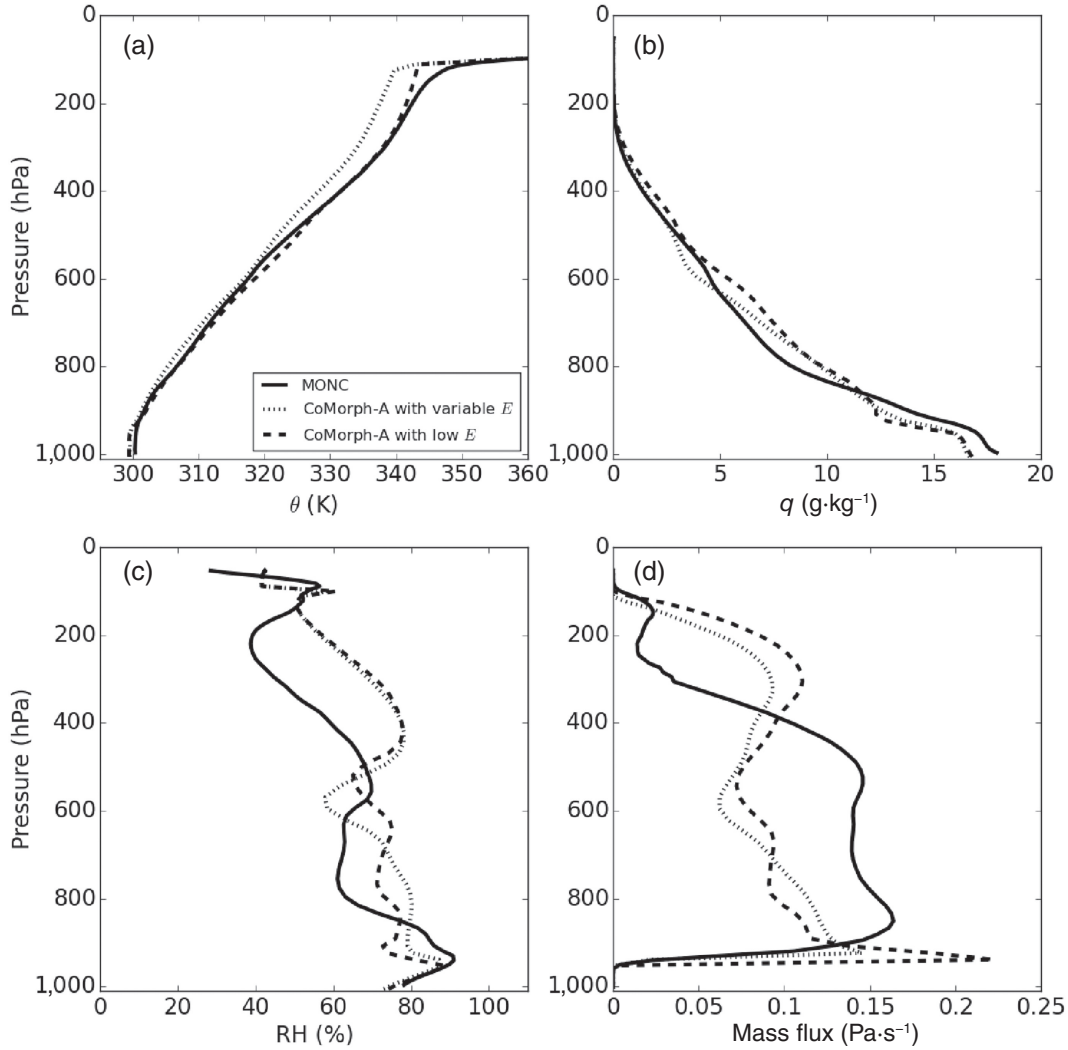

FIGURE 2 Profiles of (a) potential temperature, (b) specific humidity, (c) relative humidity, and (d) updraught mass flux obtained at equilibrium in the radiative–convective equilibrium simulations performed with the Met Office–Natural Environment Research Council cloud model (MONC; solid curves) and with the single-column model using variable (dotted curves) or low (dashed curves) E. The mass flux in MONC is shown for all cloudy updraughts.

present in the SCM (Figure 2d). This ability of MONC to precipitate as much as the SCM but at a lower CRH and the ability of the SCM to generate more deeper convection than MONC should be borne in mind when interpreting results in Section 5.

3.3 | Experimental design

The DGW simulations have the same conditions as the RCE reference state (domain size, resolutions, surface conditions, etc.) and are initialized with profiles from the RCE reference state. Using each model, we performed a DGW simulation with unperturbed temperature and moisture tendency profiles over a time interval t_0–t_1 (days 0–50).

From day 50, we imposed a stimulus forcing to temperature or moisture separately and the integrations continue up to day 100. The form of stimulus applied to temperature is

$$\left(\frac{\partial T}{\partial t}\right)_{\text{pert}} = \frac{A_T}{\tau}\sin\left(\frac{H/2 - z}{H/2}\pi\right), \quad 0 \le z \le H, \quad (7)$$

and that applied to moisture is

$$\left(\frac{\partial q}{\partial t}\right)_{\text{pert}} = \frac{A_q}{\tau}\left(\frac{z}{h}\right)^2 \exp\left[2\left(1 - \frac{z}{h}\right)\right], \quad z \ge 0, \quad (8)$$

with $H = 16\,\text{km}$, $h = 2\,\text{km}$, $A_T = \pm 1\,\text{K}$, and $A_q = \pm 0.5\,\text{g·kg}^{-1}$. Unless stated otherwise, $\tau = 1\,\text{day}$.

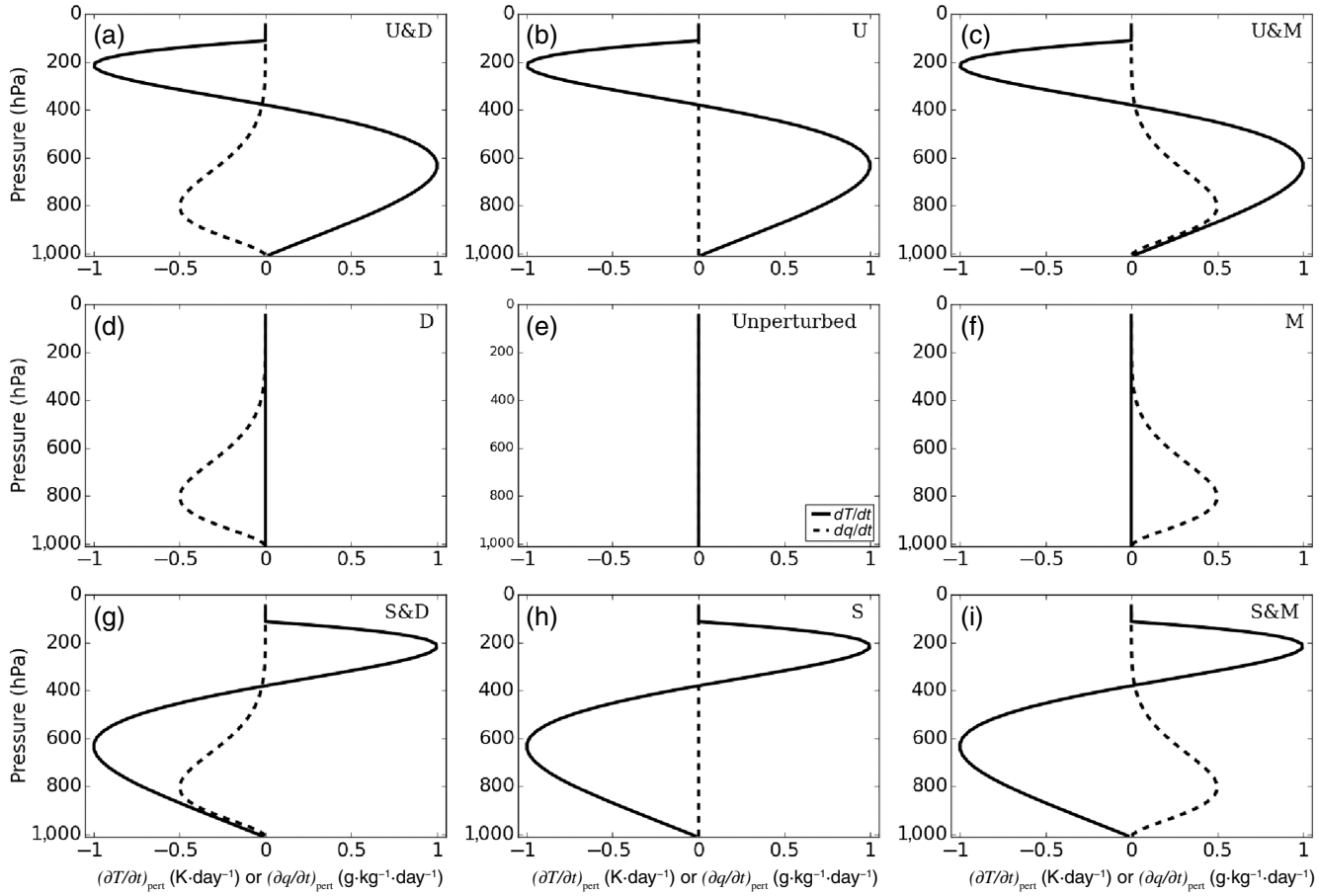

FIGURE 3 Profiles of stimulus forcing applied to temperature (solid curves) and moisture (dashed lines). (e) Unperturbed temperature and moisture tendency profiles. (a–c) Temperature stimuli enforce a less stable column (U), whereas in (g–i) they enforce a more stable column (S). (a, d, g) Moisture stimuli enforce a drier column (D), whereas in (c, f, i) they enforce a moister column (M). The legend on the top right of each panel shows modification to the temperature and/or moisture tendency profiles and they serve as legends for the results presented in Section 4. Panels (a), (c), (g), and (i) represent all possible combinations of temperature and moisture stimuli.

The background forcing (Section 2.3) sets up the basic state of convection probed in this study (the RCE reference convective state), and the temperature or moisture stimuli (Equations 7 and 8) are used to enforce a less stable (U) column (Exp1, Figure 3b), more stable (S) column (Exp2, Figure 3h), drier (D) column (Exp3, Figure 3d), or moister (M) column (Exp4, Figure 3f). The moisture stimulus peaks in the lower troposphere where humidity itself is larger and the drying tendency perturbations (Figure 3d) are similar to those imposed in the study of Wang and Sobel (2012). These amplitudes of the stimuli (A_T and A_q) are chosen to induce large convective responses. They are also chosen such that moistening or destabilizing the simulated column is equally effective in terms of enhancing precipitation in MONC (see Section 4.1.2).

We followed Sessions *et al.* (2015) and explored the full range of possible combinations of perturbations. This gives a total of eight experiments that are schematically presented in Figure 4. For each of the eight experiments, temperature and moisture stimuli are applied simultaneously from day 100 and the integrations continue up to day 150. Thus, there are dual routes for the same forcing from day 100. For one route the column is destabilized/stabilized first and then moistened/dried, and for the other the order is reversed. Among the equilibria achieved beyond day 100, we have two moister and unstable states: one that is destabilized first and then moistened (Exp1a: U&M), and the other which is moistened first and then destabilized (Exp4a: M&U). The same applies for two stable and moister states (Exp2a: S&M; and Exp4b: M&S), unstable and drier states (Exp1b: U&D; Exp3a: D&U), and stable and drier states (Exp3b: D&S; and Exp2b: S&D).

4 | RESULTS

The DGW simulations performed with the SCM using variable E also exhibit significant variations in their

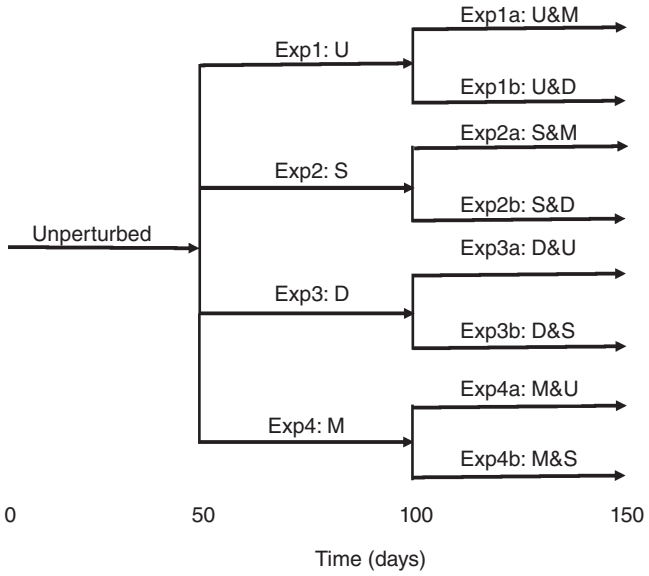

FIGURE 4 Schematic of the eight experiments representing all possible combination of temperature and moisture stimuli. Each experiment is run for 150 days. The interval 0–50 days corresponds to the damped gravity wave simulation with unperturbed temperature and moisture tendency profiles; temperature or moisture stimulus is applied separately from day 50, and applied simultaneously from day 100. U: less stable column; S: more stable column; D: drier column; M: moister column.

time series, as discussed in Section 3.2. Nevertheless, at equilibrium with or without stimulus forcings, convection characteristics are close to those obtained in equivalent simulations performed with the SCM using low E. However, some differences are found in the transient convective responses. In view of the fact these tests are performed in a single-column setting, along with the lack of time-scale within the radius ramp, which are known current limitations of the scheme (and being revised for future configurations of CoMorph), we focus instead on the performance of CoMorph-A with the setting using low E for much of the rest of the analysis, and results that show sensitivity to the entrainment formulation within CoMorph-A are discussed where appropriate.

4.1 | Approach to equilibrium

We analysed the evolution of convection within the time intervals 0–50, 50–100, and 100–150 days. The temporal evolution of precipitation is shown in Figure 5. The results are presented as the normalized precipitation rate, which is defined as the ratio of precipitation rate in the simulated column to the mean precipitation rate of the corresponding RCE reference state, $P/\overline{P}_{\mathrm{Ref}}$. In Figure 6, we also present the temporal evolution of the mass-weighted column integrated large-scale pressure velocity, $\overline{\Omega} = \int \overline{\omega}\, dp/\Delta p$. The shaded areas in Figure 5 represent precipitation rate within $^{\pm}10\%$ of $\overline{P}_{\mathrm{Ref}}$, whereas that in Figure 6 represents $\overline{\Omega}$ within $^{\pm}0.4 \times 10^{-2}$ Pa·s^{-1} (equivalent to about 10% of the radiative cooling rate imposed in the troposphere).

4.1.1 | DGW simulations with unperturbed tendency profiles

Between 0 and 50 days the time series lie mostly within the shaded areas. The equilibrium values of $P/\overline{P}_{\mathrm{Ref}}$ are 1.03 and 0.93 (or 1.01) and those of $\overline{\Omega}$ are 0.13×10^{-2} Pa·s^{-1} and -0.11×10^{-2} Pa·s^{-1} (or 0.18×10^{-2} Pa·s^{-1}) for MONC and the SCM using variable (or low) E respectively. These results indicate that the equilibrium state achieved in each model has no time-mean large-scale circulation with mean statistics close to those of its RCE reference state. Moreover, Figure 7 reveals that the resulting mean state (including that of the SCM using variable E, not shown) is also close to that of its RCE reference state. Hence, following Daleu *et al.* (2015), for each of these models the corresponding RCE state is a stable equilibrium state under the DGW mode with uniform conditions.

4.1.2 | Response to temperature or moisture stimulus

The DGW simulations with temperature or moisture stimulus applied separately start from day 50, and thus are initialized from instantaneous states that are closer to the RCE state of that same model. The stimuli drive a large-scale circulation. For each model, we carry out the integrations for 50 days, enough for the simulated column to achieve a new quasi-equilibrium state.

For each model, the new equilibrium state achieved in Exp1 and Exp4 is characterized by a large-scale ascent and enhanced precipitation compared with the unperturbed simulation. This new equilibrium state is achieved over the course of 5 days in MONC and in the SCM using variable E. However, using low E, the temporal evolution shows a rapid increase, followed by an oscillation towards the new equilibrium state. This oscillation is damped much more slowly in the SCM enforced to be less stable, and the new equilibrium state is achieved after around 30 days compared with 10 days in the SCM enforced to be moister. However, this oscillatory behaviour is sensitive to the configuration settings, as sensitivity tests reveal that it can be prevented by increasing the strength of "lateral entrainment" of the reference column air into the simulated domain.

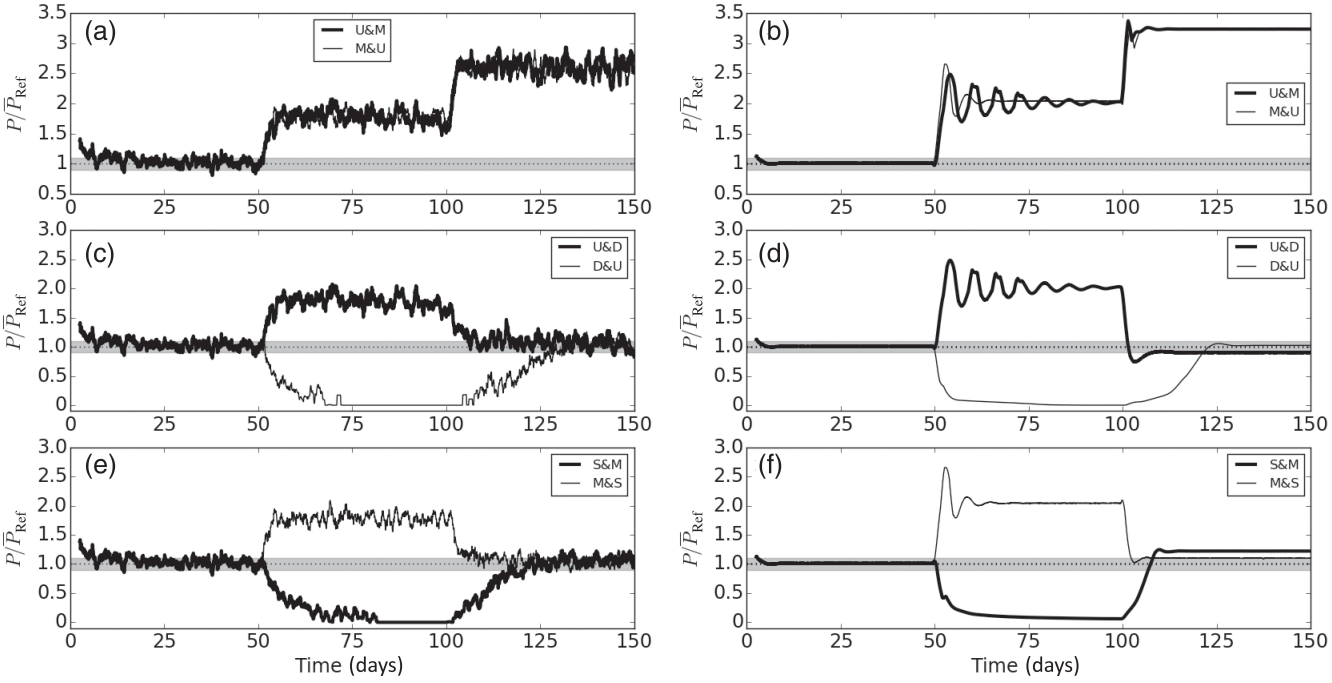

FIGURE 5 Time series of precipitation normalized by the mean value of the corresponding radiative–convective equilibrium reference column $\left(P/P_{Ref}\right)$. Results are the daily running mean obtained in the experiments conducted with (a, c, e) the Met Office–Natural Environment Research Council cloud model and with (b, d, f) the single-column model using low E. The shaded areas represent precipitation rates within $\pm 10\,\%$ of P_{Ref} . Each panel compares results from experiments applying the same combination of stimuli from day 100; one applying the moisture stimulus first (thin curves) and the other applying the temperature stimulus first (thick curves). The combination of temperature and moisture stimuli applied from day 100 is acting to (a, b) moisten and destabilize, (c, d) dry and destabilize, and (e, f) moisten and stabilize. U: less stable column; S: more stable column; D: drier column; M: moister column.

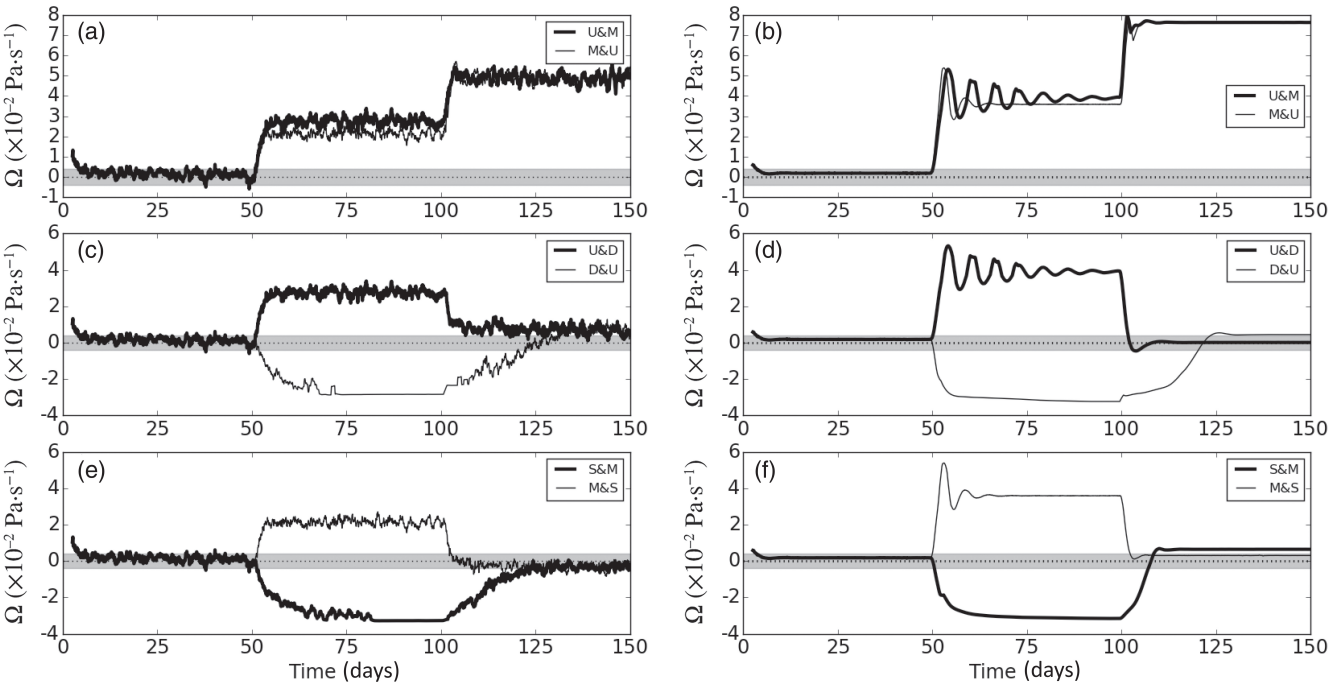

FIGURE 6 As in Figure 5, but for the mass–weighted vertical integral of the large-scale pressure velocity, $\Omega = \int \omega dp/\Delta p$. The shaded areas represent Ω within $0.4 \times 10^{-2}\ Pa.s^{-1}$ (equivalent to about 10% of the radiative cooling rate imposed in the troposphere). U: less stable column; S: more stable column; D: drier column; M: moister column.

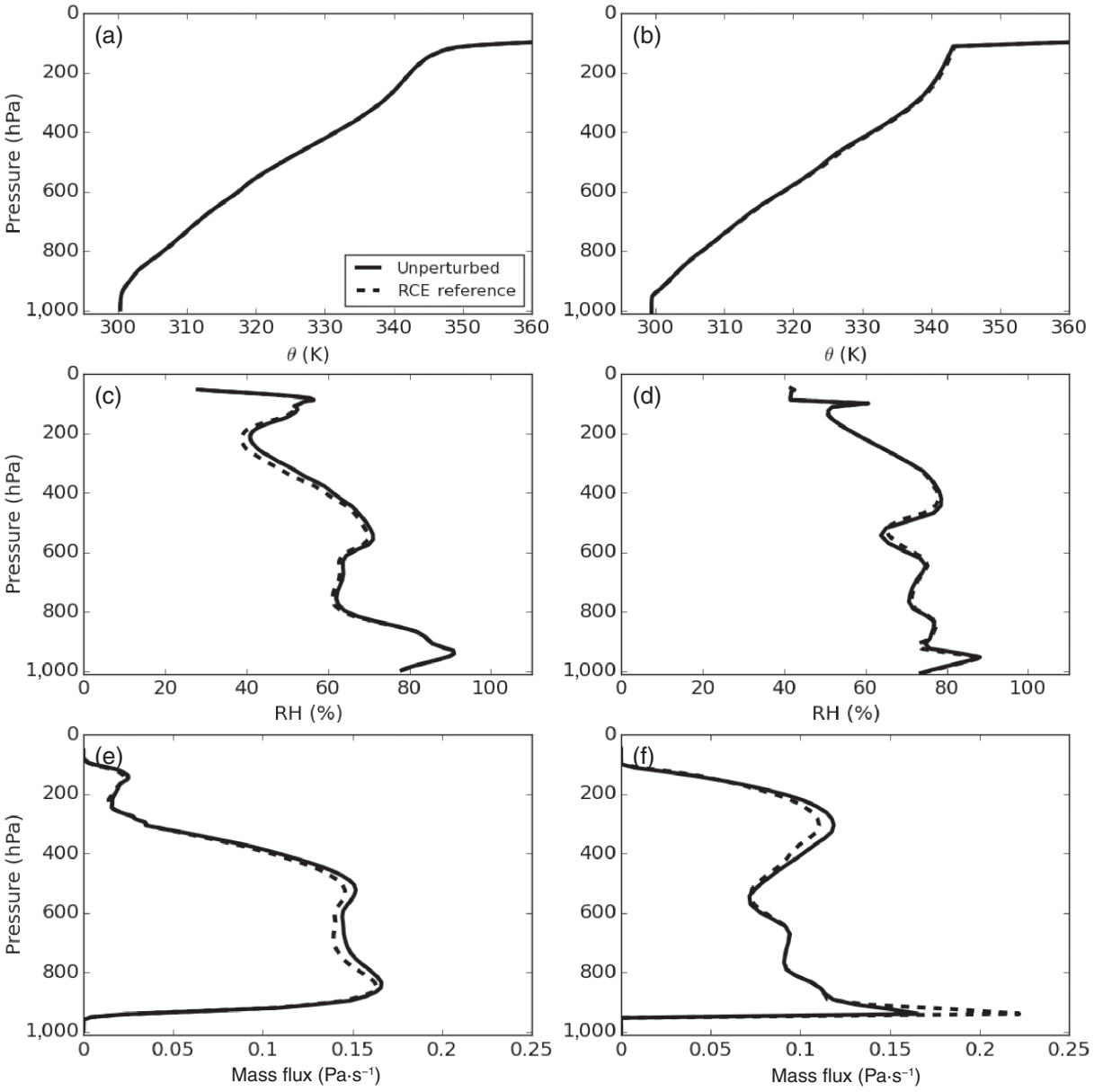

FIGURE 7 Profiles of (a, b) potential temperature (θ), (c, d) relative humidity (RH), and (e, f) updraught mass flux obtained at equilibrium in the damped gravity wave simulations with unperturbed temperature and moisture tendency profiles (solid curves). Results are shown for (a, c, e) the Met Office–Natural Environment Research Council cloud model and for (b, d, f) the single-column model using low E. Profiles from the corresponding radiative–convective equilibrium reference state (dashed curves) are shown for comparison purposes.

As noted in Section 3.3, the amplitudes of the stimuli are chosen such that the moistening or destabilization are equally effective in enhancing precipitation in MONC (Figure 5a). Similar responses are obtained in the SCM, but they are stronger for low E. For instance, using low E the SCM precipitation is increased by ≈104% with respect to its RCE reference value (now 8.7 mm·day^{-1}), compared with an ≈80% increase in MONC (now 7.48 mm·day^{-1}) and an ≈80% increase in the SCM using variable E (now 7.67 mm·day^{-1}).

For each model, drying or stabilizing the column (Exp2 or Exp3) produces a descending circulation with little or no precipitation in the column. The transition to the dry equilibrium occurs over the course of 5 days in the SCM using either low or variable E, whereas it is much slower in MONC. It occurs over around 25 days in MONC enforced to be drier and around 30 days in MONC enforced to be more stable. The overly rapid responses of the SCM suggest that CoMorph-A parametrized physics are not quite effective in capturing convective memory found in MONC simulations. In MONC and in the SCM using variable E, the large-scale descent generated from enforcing a drier or a more stable column is strong enough to shut off precipitating convection completely. In the SCM using low E,

the large-scale descent generated from enforcing a drier column also shuts off precipitating convection completely, whereas that generated from enforcing a more stable column strongly suppresses (but does not shut off) precipitating convection.

4.1.3 | Response to a combination of temperature and moisture stimuli

The DGW simulations with temperature and moisture stimuli applied simultaneously start from day 100. The integrations continue for 50 days, enough for the simulated column to achieve a new quasi-equilibrium state.

In a column enforced to be moister and less stable (Exp1a and Exp4a), the existing large-scale ascent (obtained in Exp1 or Exp4) is strengthened and precipitating convection is further enhanced, with both routes (see Section 3.3) being equally effective in enhancing precipitating convection. Using MONC, the mean precipitation rate is now 10.84 mm·day^{-1}, an increase of about 6.7 mm·day^{-1} (≈160%) compared with its RCE reference value. This increase in precipitation rate is twice that obtained in Exp1 and Exp4, indicating a linear regime with the responses equally divided between the moistening and destabilization effects. The SCM is somewhat more sensitive to a combination of moistening and destabilization effects. At equilibrium in Exp1a and Exp4a, the resulting large-scale circulation is stronger than in MONC and the equilibrium precipitation is also higher, now 12.02 mm·day^{-1} (or 13.78 mm·day^{-1}) in the SCM using variable (or low) E. That is an ≈176% (or ≈223%) increase with respect to the corresponding RCE reference value, slightly more than twice that obtained in Exp1 and Exp4.

For all models, drying a more stable column (Exp2b) or stabilizing a drier column (Exp3b) strengthens the existing large-scale descent and no convective precipitation is possible (results not shown). On the other hand, drying a less stable column (Exp1b) or stabilizing a moister column (Exp4b) weakens the existing large-scale ascent and precipitation decreases, whereas moistening a more stable column (Exp2a) or destabilizing a drier column (Exp3a) weakens the existing large-scale descent and precipitation increases. For the combinations of stimuli acting to enhance and suppress convection simultaneously (Exp1b, Exp2a, Exp3a, and Exp4b), MONC achieves equilibria with mean precipitation rates comparable to that of the corresponding unperturbed simulation (Figure 5c,e) and with either no time-mean large-scale circulation ($\Omega \approx 0$) for the moister and more stable column (Exp2a/4b; Figure 6e) or very weak column-integrated large-scale ascent for the drier and less stable column (Exp1b/3a; Figure 6c). Using the SCM, the two experiments applying the same combination of stimuli acting to enhance and suppress convection from day 100 achieve the same equilibrium state when using variable E (not shown) and two distinct precipitating equilibria, albeit with weak differences in the mean statistics when using low E (Figures 5 and 6d,f). This latter result is consistent with previous studies that found some SCMs initialized with a dry or moist state can sustain multiple stable precipitating equilibria under the DGW method (Daleu *et al.*, 2015) and could be better separated to persistent non-precipitating and precipitating equilibria under the WTG method (e.g., Sobel *et al.*, 2007; Daleu *et al.*, 2015). Despite these multiple equilibria, the mean statistics and states achieved at equilibrium in Exp1b, Exp2a, Exp3a, and Exp4b conducted with the SCM using either low or variable E are very close to those obtained in the corresponding unperturbed simulation. These results indicate that the SCM responses to a combination of stimuli acting to enhance and suppress convection simultaneously are broadly similar to those of MONC. In addition, the transient convective responses in the SCM are qualitatively similar to those in MONC, as for both models the recovery from destabilizing a drier column (Exp3a) is slower than that from moistening a more stable column (Exp2a) and recovery from a state with little or no precipitation (Exp2a/3a) is slower than that from a state with heavily precipitating convection (Exp1b/4b). However, as shown in Figure 8a, recovery from a state with little or no precipitation is sensitive to the entrainment. Compared with MONC, it is faster in the SCM using low E and overly delayed in the SCM using variable E.

We analysed the time–height cross-sections of updraught mass flux and RH in order to investigate further the transition from suppressed to active convection in each model. In MONC, when moistening a more stable state (Exp2a; Figure 8b,e) or destabilizing a drier state (Exp3a; not shown), initial shallow convective cells become more buoyant over time and ultimately accelerate throughout the middle and upper troposphere. As a result of congestus and deeper convection developing within the column, its free troposphere moistens accordingly and convective precipitation gradually increases toward its RCE reference value. This process is faster in the SCM using low E, as convection rapidly extends throughout the upper troposphere (compare Figure 1b,c). However, it is overly delayed in the SCM using variable E because the convection top is limited below 600 hPa for over 30 days, before extending rapidly throughout the upper troposphere.

4.2 | Vertical profiles at equilibrium

From Figures 5 and 6, the time-scale of adjustment to a new quasi-equilibrium state with the parametrized

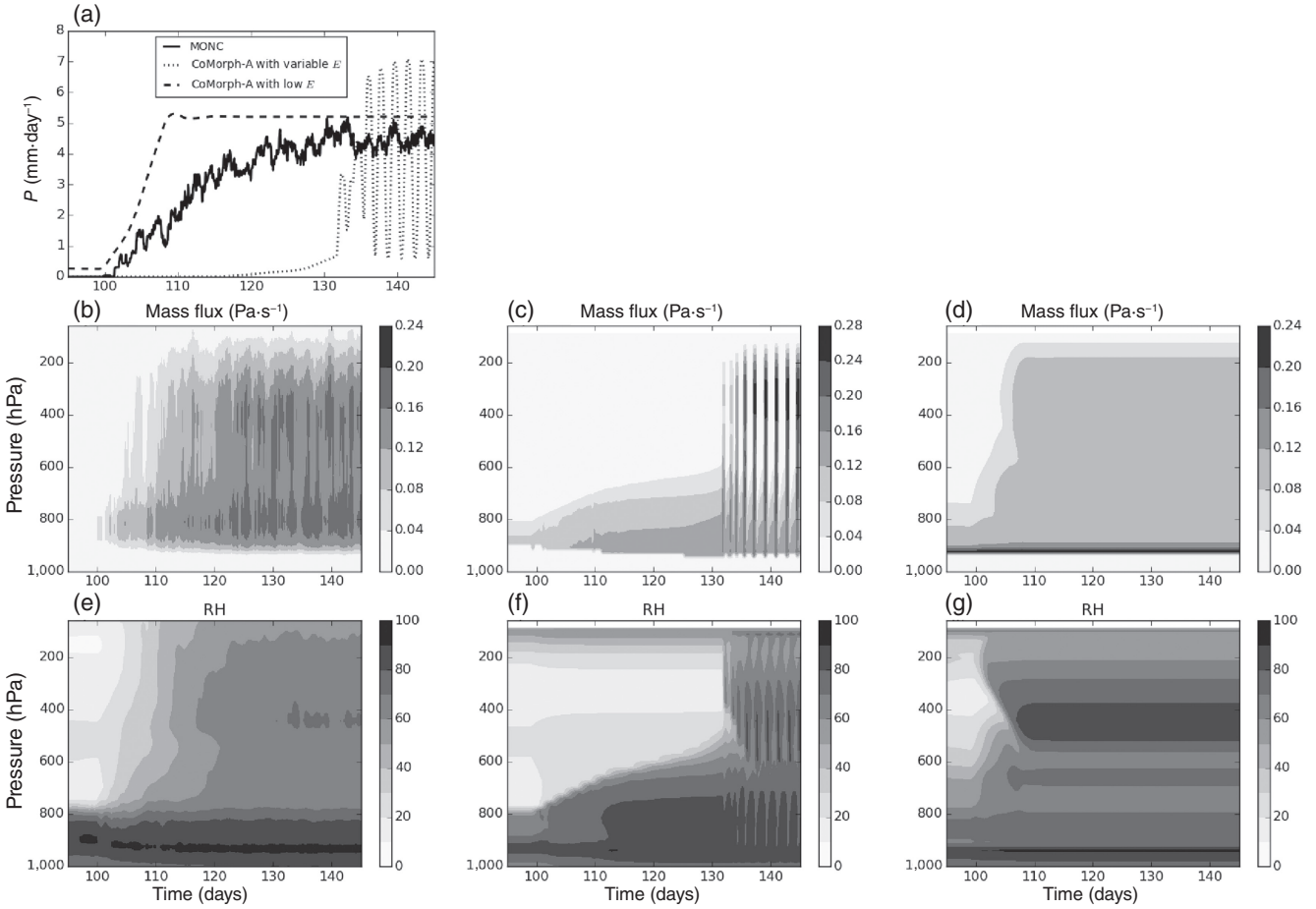

FIGURE 8 (a) Time series of precipitation and (b–g) time–height cross-sections of (b, c, d) updraught mass flux and (e, f, g) relative humidity (RH, %). Results are the daily running mean obtained in Exp2a conducted with (b, e; a, solid curve) the Met Office–Natural Environment Research Council cloud model (MONC) and with (c, f; a, dotted curve) the single-column model using variable E or (d, g; a, dashed curve) the single-column model using low E.

large-scale circulation and with temperature and/or moisture stimuli ranges between 5 and 30 days, depending on the model and on which thermodynamic tendency profile is perturbed. Thus, the mean statistics discussed in Section 4.1 and the mean states to be discussed here have been obtained by averaging over the last 20 days of the 50-day integrations. Figures 9,10, and 11 show profiles at equilibrium of $\overline{\omega}$, RH, and updraught mass flux respectively.

For all models, enforcing a less stable (more stable) column generates a large-scale ascent (descent) throughout the free troposphere which enhances (completely shuts off) deep convection, and the column becomes relatively moist (dry) with respect to the equilibrium state achieved in the unperturbed simulation. Moistening the less stable column strengthens the existing large-scale ascent and convective activities are further enhanced (compare Exp1 and Exp1a/4a in Figure 11a,b). The large-scale pressure velocities generated by both models have similar shapes with peaks around 300 hPa. As discussed in section 4.1.3, the SCM is more sensitive to a combination of stimuli acting to enhance convection and this is reflected in its large-scale pressure velocity which is stronger and top–heavier, compared to that in MONC (compare Figure 9a with Figure 9b,c).

When drying a more stable column, the existing large-scale descent remains relatively unchanged in MONC and in the SCM using variable E (Figure 9j,k), whereas that in the SCM using low E becomes more bottom heavy (Figure 9l) and shuts off precipitating convection completely. Note that radiative cooling and temperature and moisture stimuli are fixed and have the same strength for all models. In addition, in this study, the changes in surface fluxes due to perturbations in near-surface winds enforced by changes in convective activity are somewhat constrained by imposing a mean surface wind in the surface flux calculations. Thus, in a non-convective equilibrium, the heating and moistening induced by $\overline{\omega}$ are expected to have comparable values for all models, and this is reflected in the large-scale pressure

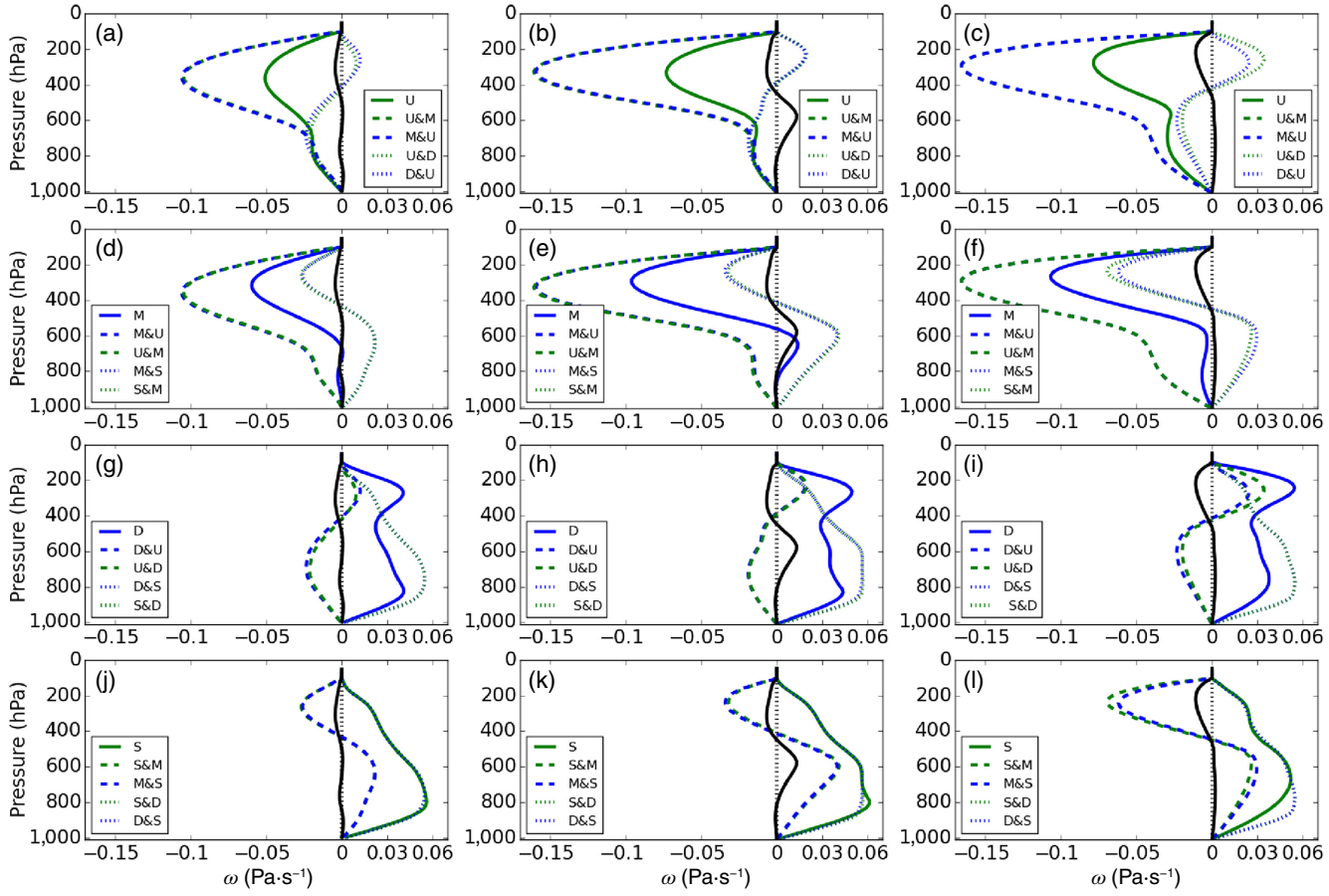

FIGURE 9 Profiles of the large-scale pressure velocity. Results are those obtained at equilibrium in the damped gravity wave (DGW) simulations performed with (a, d, g, j) the Met Office–Natural Environment Research Council cloud model (MONC) and with (b, e, h k) the single-column model using variable or (c, f, i, l) low E, with temperature or moisture stimulus forcing applied separately (solid curves), and with temperature and moisture stimuli applied simultaneously (dotted/dashed curves). Profiles from the corresponding radiative–convective equilibrium reference state and profiles at equilibrium in the corresponding DGW simulation with unperturbed temperature and moisture tendency profiles are shown for comparison purposes. U: less stable column; S: more stable column; D: drier column; M: moister column.

velocity profiles, which have similar shapes and strengths (compare Figure 9j,k,l).

When drying a less stable column, convective activity is reduced and the existing large-scale ascent weakens below 400 hPa and switches to large-scale descent aloft (compare Exp1 and Exp1b in Figures 9a,b,c and 11a,b). Analysis of time–height cross-sections (not shown) reveals that, when dry tendencies start to be applied in a less stable column, convective cells entraining drier air decelerate and the existing large-scale ascent weakens accordingly. Some of the convective cells become neutrally buoyant more readily, limiting the depth of convection. As a result of fewer cells extending above 400 hPa, the upper troposphere rapidly cools down and develops a large-scale descent once it becomes colder than its reference state. On the other hand, when moist tendencies start to be applied within a more stable column, the shallow convective cells become more buoyant due to the entrainment of moister air and accelerate faster throughout the free troposphere, and the existing large-scale descent weakens accordingly. As a result of more convective clouds extending above 400 hPa, the upper troposphere warms up and a large-scale ascent develops once it becomes warmer than its reference state (compare Exp2 and Exp2a in Figure 9j,k,l).

For all models, applying drying tendencies generate large-scale descent at all levels, with very low tropospheric RH and a column emptied of deep convection (Exp4 in Figures 10e,f and 11e,f). This result is consistent with that of Wang and Sobel (2012) who found that injecting dry air in the lower troposphere can prevent the column from generating deep convection. For all models, the existing large-scale descent becomes more bottom–heavy when stabilizing the drier column and shallow non–precipitating convection is further suppressed (Exp3 and Exp3b/2b in Figures 9g,h,i and 11e,f). On the other hand, when destabilizing the drier column,

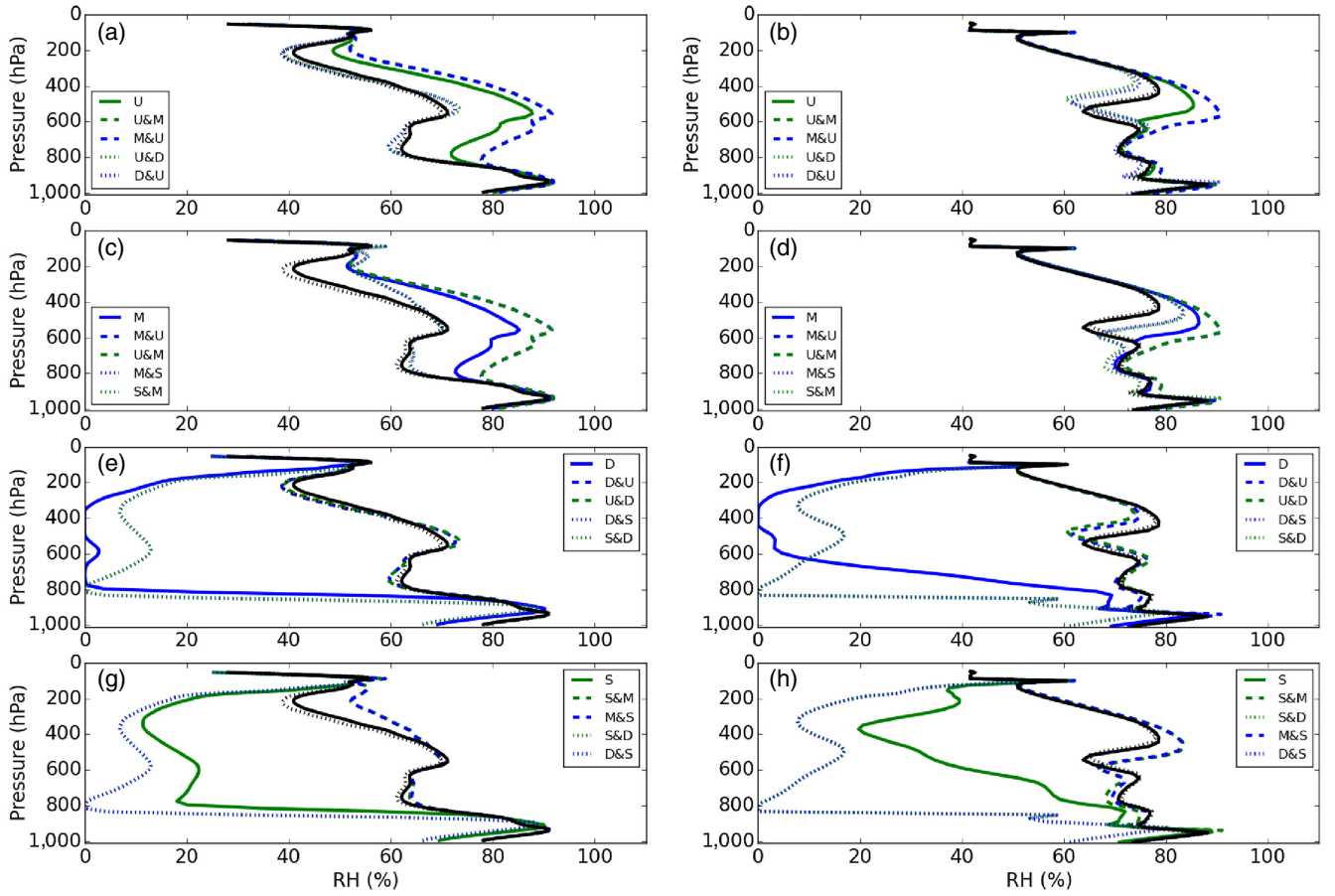

FIGURE 10 Profiles of relative humidity. Results are those obtained at equilibrium in the damped gravity wave (DGW) simulations performed with (a, c, e, g) the Met Office–Natural Environment Research Council cloud model (MONC) and with (b, d, f, h) the single-column model using low E, with temperature or moisture stimulus forcing applied separately (solid curves), and with temperature and moisture stimuli applied simultaneously (dotted/dashed curves). Profiles from the corresponding radiative–convective equilibrium reference state and profiles at equilibrium in the corresponding DGW simulation with unperturbed temperature and moisture tendency profiles are shown for comparison purposes. U: less stable column; S: more stable column; D: drier column; M: moister column.

the large-scale circulation below 400 hPa switches from descent to ascent and the shallow non–precipitating cells become more buoyant accelerating upward throughout the less stable column (Exp3 and Exp3a in Figure 9g,h,i).

A moister column generates a large-scale ascent above 600 hPa with either a negligible (for MONC) or weaker large-scale circulation (for the SCM) underneath (Figure 9d,e,f). For all models, destabilizing (stabilizing) the moister column strengthens (weakens) the existing large-scale ascent in the upper troposphere and generates a large-scale ascent (descent) underneath (Exp4, Exp4a/4b in Figure 9d,e,f). The lower tropospheric large-scale ascent (descent) accelerates (decelerates) the buoyant cells and convection becomes more (less) active compared with the equilibrium state in Exp4 (Figure 11c,d).

All models show similar sensitivity to stimuli acting to suppress convection. Even though the SCM using low E shows stronger sensitivity to stimuli acting to enhance convection, for all models the experiments applying any combination of stimuli acting to enhance and suppress convection simultaneously settle to equilibrium states with convection intensity and vertical structure close to those of the corresponding unperturbed simulation.

Note that the large-scale circulation below 600 hPa is not sensitive to the suppression (enhancement) of convection induced by the drying (moistening) stimulus for MONC enforced to be less stable. A similar result is obtained in the SCM using variable E, whereas the SCM using low E shows a weakening (strengthening) of the large-scale circulation below 600 hPa when drying (moistening) stimulus is applied in a less stable column (compare Figure 9c with Figure 9a,b). Nevertheless, the large-scale circulations generated by all models have similar shapes, but those generated by the SCM are generally stronger, particularly in the upper troposphere. Overall, for the combination of stimuli, the direction of the large-scale circulation below 400 hPa is governed by the sign of temperature stimulus within those levels, whereas that

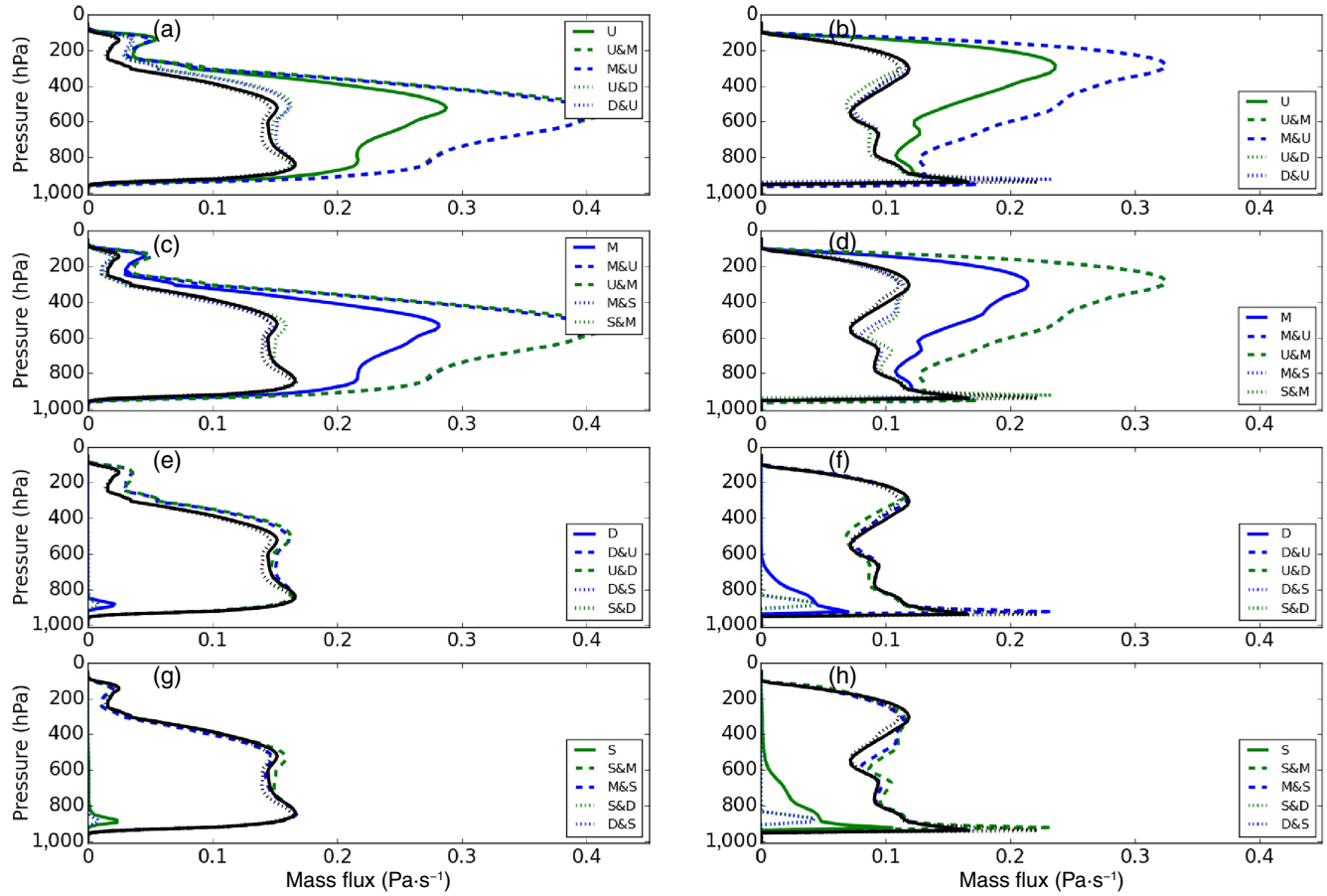

FIGURE 11 As in Figure 10, but for updraught mass flux. U: less stable column; S: more stable column; D: drier column; M: moister column.

aloft is governed by the sign of the moisture stimulus. This is illustrated by noting that a less stable (more stable) column generates large-scale ascent (descent) below 400 hPa, independent of the moisture stimulus applied, whereas a moister (drier) column generates large-scale ascent (descent) above 400 hPa, independent of the temperature stimulus applied (e.g., Exp1b; dotted green curves in Figure 9a,b,c).

5 | CONVECTIVE RESPONSE AS A FUNCTION OF THE STRENGTHS OF MOISTURE STIMULI

We evaluate the convective responses in a set of experiments in which moisture stimuli with various strengths are applied from t_1. The time-scale τ in Equation (8) is varied between 3 hr and 10 days. The integrations continue for 50 days, and the last 20 days of each experiment are averaged to define the mean statistics discussed here. As in Section 4, we present results from the SCM using low E, and results that show sensitivity to the entrainment formulation within CoMorph-A are discussed where appropriate.

To provide a more quantitative evaluation of convective responses, we calculated the vertical integral of the moisture stimulus applied; that is,

$$E_q = \int \left(\frac{\partial q}{\partial t}\right)_{\text{pert}} dp/g,$$

where g denotes the acceleration due to gravity. Here, positive (negative) values of E_q correspond to moist static energy import by moistening (export by drying). Figure 12a shows scatter plots of the changes in convective precipitation with respect to the RCE reference value ($\Delta\overline{P} = \overline{P} - \overline{P}_{\text{Ref}}$) versus E_q. We expressed E_q in millimetres per day via the density of water in order to allow easy comparison with the precipitation rates. From the moisture budget equation, $\Delta\overline{P}$ must be equal to the sum of changes in evaporation with respect to the RCE reference value ($\Delta\overline{E} = \overline{E} - \overline{E}_{\text{Ref}}$), the moistening rate due to the derived large-scale circulation, and the applied E_q. However, as stated in Section 4.1.3, we have constrained the

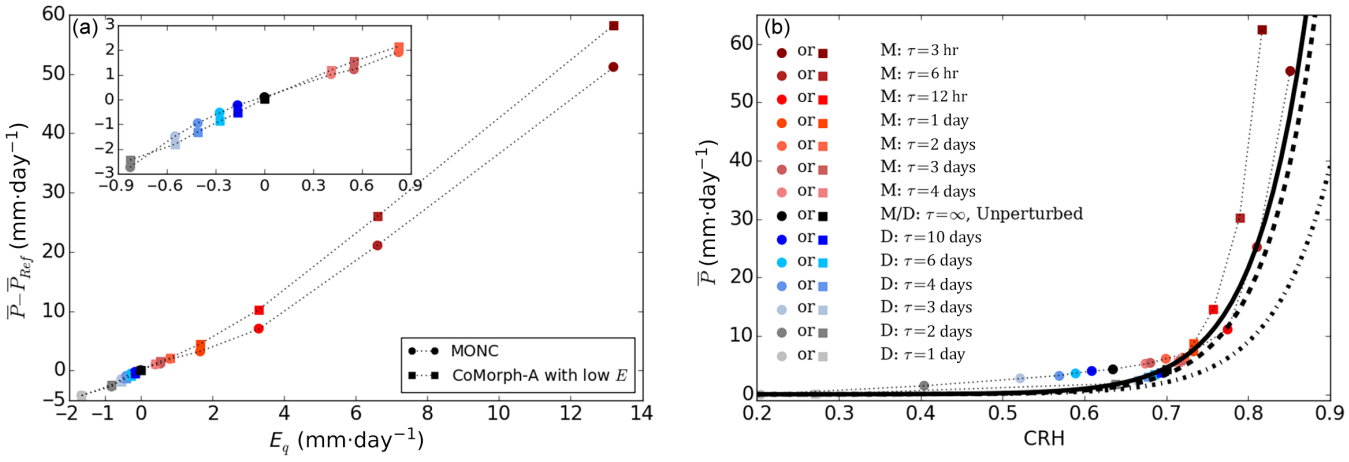

FIGURE 12 (a) Scatter plots of the changes in mean precipitation rates with respect to the radiative–convective equilibrium reference value ($\overline{\Delta P} = \overline{P} - \overline{P}^{Ref}$) and column–integrated moist static energy import or export due to the imposed moisture stimulus (E_q). E_q is expressed in millimetres per day via the density of water. The inset in panel (a) shows results for moderate moisture stimuli ($|E_q| \leq 0.83$ mm. d^{-1}−1 or $\tau \geq 2$ days). (b) Scatter plots of P versus column relative humidity (CRH; the column-integrated water vapour divided by its saturation value). Results in panels (a) and (b) are those obtained at equilibrium in simulations applying moisture stimuli of different strengths as indicated by the colour legend in (b). For both panels, results from the Met Office–Natural Environment Research Council cloud model (MONC) are represented using full circles and those from the single-column model are represented using full squares. The thick curves (solid, dashed, dashed-dotted) in (b) are exponential fits for the observed daily mean precipitation over the tropical oceans. The solid curve is derived by Bretherton et al. (2004) using the version 5 Special Sensor Microwave Imager (SSMI) data, the dashed curve is the revision of the solid curve by Rushley et al. (2018), and the dashed-dotted curve is derived by Rushley et al. (2018) using the version 7 (upgraded from version 5) SSMI data. D: drier column; M: moister column.

calculations of surface fluxes in our study, and analysis reveals that $\Delta\overline{E}$ is generally much smaller than $\Delta\overline{P}$ (not shown). For all energy imports/exports exceeding 0.165 mm·day^{-1} ($\tau < 10$ days), we also find that E_q is less than two-fifths of $\Delta\overline{P}$. These results imply that changes in convective precipitation are mostly driven by the derived large-scale vertical motion.

In MONC, a precipitating equilibrium is possible for moderate energy exports ($E_q \geq -0.83$ mm·day^{-1}, or $\tau \geq 2$ days). For moderate energy export/import ($|E_q| \leq 0.83$ mm·day^{-1}; Figure 12a inset), a roughly linear relationship between precipitation and E_q is obtained. This $\overline{P}$ versus E_q relationship is qualitatively similar to that obtained by Wang and Sobel (2012) when imposing drying tendencies of different strength in vertical layers between 825 and 600 hPa of a CRM coupled to WTG-derived large-scale circulation. In the SCM using variable E (not shown), a precipitating equilibrium is not possible for $E_q < -0.41$ mm·day^{-1} (or $\tau < 4$ days), and the changes in precipitation are very close to those in MONC for all moistening and for drying up to 0.28 mm·day^{-1}. On the other hand, the changes in precipitation in the SCM using low E are very close to those in MONC for all drying and for moistening up to 0.83 mm·day^{-1}, above which they are stronger.

Figure 12b shows scatter plots of precipitation versus CRH simulated using both models and the exponential curve of the form $P\,(\text{mm}\cdot\text{day}^{-1}) = \exp[15.6(\text{CRH} - 0.603)]$ that describes the relationship between precipitation and CRH derived from the version 5 Special Sensor Microwave Imager observations over the tropical oceans (Bretherton *et al.*, 2004). It also shows two additional curves obtained by Rushley *et al.* (2018). One of the curves has the form $P\,(\text{mm}\cdot\text{day}^{-1}) = 4.07 \times 10^{-5} \exp(16.12 \times \text{CRH})$ and is the revision of that found by Bretherton *et al.* (2004), and the other has the form $P\,(\text{mm}\cdot\text{day}^{-1}) = 6.89 \times 10^{-5} \exp(14.72 \times \text{CRH})$ and is derived using the version 7 (upgraded from version 5) Special Sensor Microwave Imager data.

For moderate energy import/export, analysis reveals that MONC is warmer and moister below 850 hPa, but its CRH is lower than in the SCM because its free troposphere is generally drier (e.g., Figure 2). As discussed in section 3.2, MONC at lower CRH precipitates as much as the SCM because it generates more active precipitating shallow and congestus convection than the SCM. However, for stronger energy imports (Eq ≥ 1.65 $mm.d^{-1}$) MONC has higher CRH than in the SCM because its layer above 600 hPa is equally as moist as in the SCM but its layer underneath is moister. Despite these quantitative differences, the precipitation–CRH relationships simulated using both models qualitatively resemble the observed exponential fits and the relationships found in other idealised numerical studies (e.g., Bretherton et al., 2004; Wang and Sobel,

2011; Rushley et al., 2018; Kuo et al., 2020). For all models, P increases monotonically with CRH and there is a threshold below which only weak precipitation is permitted, and above which a significant increase in precipitation is obtained, followed by a sharp pickup of precipitation for small increase in CRH. From observations, the CRH threshold varies between 75–80% (thick curves in Figure 12b, Bretherton et al., 2004; Rushley et al., 2018). For all models, the precipitation pickup occurs around CRH threshold that is closer to the lower end of the range obtained in observations.

Below the threshold, the precipitation–CRH relationship in the SCM is closer to the lower end of the curves derived from observations, presumably because the SCM generates more deeper convection, as observed over the tropical oceans. However, in MONC, shallow and congestus convection are the dominant modes, and this significantly affects its precipitation–CRH relationship. Note that the observed data points with very low precipitation correspond to large-scale subsidence over warm sea-surface-temperature areas in the Tropics, and this is not consistent with the simulation settings used in this study. Therefore, below the threshold we do not expect a very good match between the observed and simulated precipitation–CRH relationships. Above the threshold, the CRH in MONC is higher than in the SCM, but shallow and congestus convection remain important modes. However, though the precipitation–CRH relationship simulated using MONC is closer to the lower end of the curves derived from observations, precipitation in the SCM using either low or variable E rises more abruptly for small increases in CRH above the threshold. This abrupt increase of precipitation in the SCM is informative. It suggests that CoMorph-A parametrized physics do not appropriately capture the precipitation–CRH relationship as the CRH increases passes its threshold.

6 | CONCLUSIONS

A CRM and an SCM are modified to implement the DGW method using a configuration that couples each model to a predefined reference state. The CRM used is MONC. The SCM is a one-column version of the idealized configuration of the Met Office Unified Model, using the new convection parametrization scheme CoMorph-A. The entrainment rate within CoMorph-A varies as a function of convective size, and this is set to depend on the precipitation rate from the previous time step. We explored the sensitivity of this formulation by comparing with entrainment set to its lowest value, consistent with the simulation of deep convective cells. For each model, the reference state is obtained from the previous RCE simulation of that same model, and analysis revealed that simulations under the DGW method with uniform conditions achieved the same RCE reference state with no time-mean large-scale circulation.

In previous studies examining convective responses, perturbations of the simulated column have been introduced by adding continuous drying (e.g., Sobel and Bellon, 2009; Wang and Sobel, 2012) or by imposing anomalies to the moisture and atmospheric stability over a short period of the simulations (e.g., Mapes, 2004). In the present study, stimulus forcings are applied continuously to mimic advection of cold/warm and/or dry/moist air into the simulated region.

In this study, the amplitudes of the stimuli were deliberately set to ensure that moistening or destabilizing reached similar solutions in MONC. In the SCM, enforcing a moister or less stable column is also equally effective in enhancing precipitating convection, and the new equilibria achieved are similar to those in MONC. However, using low entrainment, the SCM responses are stronger and the time of adjustment to the new equilibria is longer, and much longer if the SCM is enforced to be less stable. MONC enforced to be drier or a more stable column generates uniform large-scale descent that prevents deep convection and shuts off precipitation completely. A similar result was also obtained by Wang and Sobel (2012) when injecting dry air in the lower troposphere. The SCM enforced to be drier or more stable adjusts to dry equilibria that are similar to those in MONC. However, its transient rainfall responses are markedly too fast, and this is likely to be due to the inability of CoMorph-A parametrized physics to adequately capture the long-term memory properties found in MONC simulations.

Convection responses are mainly driven by the induced large-scale motion. For a combination of stimuli, the temperature stimulus prescribes the direction of the large-scale circulation in the lower and middle troposphere, whereas the moisture stimulus prescribes the direction of the large-scale circulation aloft. The fact that the moisture stimulus governs the sign of the large-scale circulation at upper levels where moisture is not important is a surprising result. As a future study, we may investigate whether it is a typical behaviour of CoMorph coupled to any large-scale parametrization method or if a similar behaviour is obtained when using other convection parametrization schemes. For a combination of stimuli acting to enhance convection, the resulting large-scale ascent in the SCM is stronger and more top heavy than in MONC. As a result, convection responses are also stronger. Compared with simulations that apply moistening or destabilization separately, precipitation responses are doubled in MONC and more than doubled in the SCM. Finally, convection characteristics at equilibrium in the SCM are

relatively insensitive to a combination of stimuli simultaneously acting to enhance and suppress convection, in agreement with MONC. However, using variable entrainment, the SCM recovery from a non-precipitating state is overly delayed, whereas a recovery time shorter than that in MONC is obtained when using low entrainment.

We also explored the responses to moisture stimuli of different strengths. For moderate energy import/export, the precipitation versus energy import/export relationships in MONC are roughly linear. Convective responses in the SCM using variable entrainment are very similar to those in MONC for all moistening and drying up to 0.28 mm·day^{-1}, below which dry equilibria with little or no precipitation are obtained. On the other hand, convective responses in the SCM using low entrainment are similar to those in MONC for all drying and for moistening up to 0.83 mm·day^{-1}, above which they are stronger.

For both models, precipitation increases monotonically with CRH, and there is a CRH threshold below which only weak precipitation is permitted and above which a sharp pick-up of precipitation is obtained for small increase in CRH. This relationship qualitatively resembles that seen in observations and those found in other idealized studies (e.g., Bretherton *et al.*, 2004; Wang and Sobel, 2011; Rushley *et al.*, 2018). For both models, precipitation pick-up occurs around a CRH threshold at the lower end of the range obtained in observations. (Bretherton *et al.*, 2004; Rushley *et al.*, 2018). Below the threshold, the precipitation–CRH relationship in the SCM is the closest to the curves derived from observations. The SCM generates more deeper convection, as observed over the tropical oceans, whereas shallow and congestus convection are the dominant modes in MONC, and this significantly affects the simulated precipitation–CRH relationship. Above the threshold, the CRH in MONC is higher than in the SCM. Shallow and congestus convection remain important modes in MONC, and its simulated precipitation–CRH relationship is the closest to the curves derived from observations. However, precipitation in the SCM using variable or low entrainment rises more abruptly than in MONC and observations, indicating that CoMorph-A parametrized physics do not appropriately capture the increase of column humidity with precipitation as the former increases passes its threshold.

This study has evaluated the SCM using CoMorph-A against MONC, using a configuration that couples convection to parametrized large-scale dynamics with non-interactive radiation and a non-interactive surface. Further study may include the sensitivity to interactive radiation and/or an interactive surface. Comparisons between the SCM and MONC under parametrized large-scale dynamical feedback allow an assessment of the ability of SCM parametrized physics to capture the appropriate convective responses and highlight behaviours of the SCM that would not have been found in a traditional SCM setting. Overall, the SCM steady responses to stimulus forcings under the influence of evolving large-scale dynamics are broadly similar to those in MONC. However, compared with MONC, precipitation in the SCM rises more abruptly for small increase in CRH above the threshold, and the transition from suppressed to enhance precipitating convection is overly delayed when using variable entrainment. These differences in behaviours (alongside results from other idealized NWP and GCM tests on which we and other collaborators intend to report in further articles) have highlighted the need to further develop CoMorph-A. Future versions of CoMorph are intended to include a reformulation of the entrainment (including a dynamical contribution due to vertical acceleration, and reconsideration of the precipitation ramp), the introduction of a second convective mode (associated with forced uplift), and a treatment of stochastic variability.

AUTHOR CONTRIBUTIONS

Chimene L. Daleu: conceptualization; data curation; formal analysis; investigation; methodology; writing – original draft; writing – review and editing. **Robert S. Plant:** conceptualization; funding acquisition; resources; supervision; validation; visualization. **Alison J. Stirling:** funding acquisition; investigation; resources; supervision; validation. **Mike Whitall:** formal analysis; investigation; resources.

ACKNOWLEDGEMENTS

Chimene Daleu and Robert Plant gratefully acknowledge funding from NERC grant NE/N013743/1, which was part of the ParaCon programme. We acknowledge use of the NEXCS system, a collaborative facility supplied under the Joint Weather and Climate Research Programme, a strategic partnership between the Met Office and the Natural Environment Research Council. The model data from the experiments performed in this study and the scripts used to analyze those data are available in a Zenodo repository (https://zenodo.org/deposit/8200007).

ORCID

Chimene L. Daleu https://orcid.org/0000-0003-2075-4902
Robert S. Plant https://orcid.org/0000-0001-8808-0022

REFERENCES

Bretherton, C.S., Peters, M.E. and Back, L.E. (2004) Relationships between water vapor path and precipitation over the tropical oceans. *Journal of Climate*, 17(7), 1517–1528.

Bretherton, C.S. and Smolarkiewicz, P.K. (1989) Gravity waves, compensating subsidence and detrainment around cumulus clouds. *Journal of Atmospheric Sciences*, 46(6), 740–759.

Brown, N., Weiland, M., Hill, A., Shipway, B., Maynard, C., Allen, T. and Rezny, M. (2020) A highly scalable met office nerc cloud model. arXiv preprint arXiv:2009.12849.

Daleu, C.L., Plant, R.S. and Woolnough, S.J. (2017) Using the weak-temperature gradient approximation to evaluate parameterizations: an example of the transition from suppressed to active convection. *Journal of Advances in Modeling Earth Systems*, 9(6), 2350–2367.

Daleu, C.L., Plant, R.S., Woolnough, S.J., Sessions, S., Herman, M.J., Sobel, A., Wang, S., Daehyun Kim, A. and Cheng, G.B. (2015) Intercomparison of methods of coupling between convection and large-scale circulation: 1. Comparison over uniform surface conditions. *Journal of Advances in Modeling Earth Systems*, 7(4), 1576–1601.

Daleu, C.L., Plant, R.S., Woolnough, S.J., Sessions, S., Herman, M.J., Sobel, A., Wang, S., Daehyun Kim, A. and Cheng, G.B. (2016) Intercomparison of methods of coupling between convection and large-scale circulation: 2. Comparison over nonuniform surface conditions. *Journal of Advances in Modeling Earth Systems*, 8(1), 387–405.

Daleu, C.L., Plant, R.S., Woolnough, S.J., Stirling, A.J. and Harvey, N.J. (2020) Memory properties in cloud-resolving simulations of the diurnal cycle of deep convection. *Journal of Advances in Modeling Earth Systems*, 12, e2019MS001897. https://doi.org/10.1029/2019MS001897.

Daleu, C.L., Woolnough, S.J. and Plant, R.S. (2012) Cloud-resolving model simulations with one-and two-way couplings via the weak temperature gradient approximation. *Journal of the Atmospheric Sciences*, 69(12), 3683–3699.

Dearden, C., Hill, A., Coe, H. and Choularton, T. (2018) The role of droplet sedimentation in the evolution of low-level clouds over southern west africa. *Atmospheric Chemistry and Physics*, 18(19), 14253–14269.

Derbyshire, S.H., Beau, I., Bechtold, P., Grandpeix, J.-Y., Piriou, J.-M., Redelsperger, J.-L. and Soares, P.M.M. (2004) Sensitivity of moist convection to environmental humidity. *Quarterly Journal of the Royal Meteorological Society: A Journal of the Atmospheric Sciences, Applied Meteorology and Physical Oceanography*, 130(604), 3055–3079.

Edman, J.P. and Romps, D.M. (2014) An improved weak pressure gradient scheme for single-column modeling. *Journal of the Atmospheric Sciences*, 71(7), 2415–2429.

Endris, H.S., Hirons, L., Segele, Z.T., Gudoshava, M., Woolnough, S. and Artan, G.A. (2021) Evaluation of the skill of monthly precipitation forecasts from global prediction systems over the greater horn of africa. *Weather and Forecasting*, 36(4), 1275–1298.

Ferrett, S., Frame, T.H.A., Methven, J., Holloway, C.E., Webster, S., Stein, T.H.M. and Cafaro, C. (2021) Evaluating convection-permitting ensemble forecasts of precipitation over southeast asia. *Weather and Forecasting*, 36(4), 1199–1217.

Grabowski, W.W., Xiaoqing, W. and Moncrieff, M.W. (1996) Cloud-resolving modeling of tropical cloud systems during phase iii of gate. Part i: two-dimensional experiments. *Journal of the Atmospheric Sciences*, 53(24), 3684–3709.

Gregory, D. and Rowntree, P.R. (1990) A mass flux convection scheme with representation of cloud ensemble characteristics and stability-dependent closure. *Monthly Weather Review*, 118(7), 1483–1506.

Grosvenor, D.P., Field, P.R., Hill, A.A. and Shipway, B.J. (2017) The relative importance of macrophysical and cloud albedo changes for aerosol-induced radiative effects in closed-cell stratocumulus: insight from the modelling of a case study. *Atmospheric Chemistry and Physics*, 17(8), 5155–5183.

Gu, J-F., Plant, R.S., Holloway, C.E., Jones, T.R., Stirling, A., Clark, P.A., Woolnough, S.J. and Webb, T.L. (2020) Evaluation of the bulk mass flux formulation using large-eddy simulations. *Journal of the Atmospheric Sciences*, 77(6), 2115–2137.

Haslebacher, C., Demory, M.-E., Demory, B.-O., Sarazin, M. and Vidale, P.L. (2022) Impact of climate change on site characteristics of eight major astronomical observatories using high-resolution global climate projections until 2050. arXiv preprint arXiv:2208.04918.

Herman, M.J. and Kuang, Z. (2013) Linear response functions of two convective parameterization schemes. *Journal of Advances in Modeling Earth Systems*, 5(3), 510–541.

Herman, M.J. and Raymond, D.J. (2014) Wtg cloud modeling with spectral decomposition of heating. *Journal of Advances in Modeling Earth Systems*, 6(4), 1121–1140.

Hertwig, D., Ng, M., Grimmond, S., Vidale, P.L. and McGuire, P.C. (2021) High-resolution global climate simulations: representation of cities. *International Journal of Climatology*, 41(5), 3266–3285.

Hill, A.A., Shipway, B.J. and Boutle, I.A. (2015) How sensitive are aerosol-precipitation interactions to the warm rain representation? *Journal of Advances in Modeling Earth Systems*, 7(3), 987–1004.

Holloway, C.E., Woolnough, S.J. and Lister, G.M.S. (2012) Precipitation distributions for explicit versus parametrized convection in a large-domain high-resolution tropical case study. *Quarterly Journal of the Royal Meteorological Society*, 138(668), 1692–1708.

Hwong, Y.-L., Siwon Song, S.C., Sherwood, A.J.S., Rio, C., Roehrig, R., Daleu, C.L., Plant, R.S., Fuchs, D. and Maher, P. (2021) Characterizing convection schemes using their responses to imposed tendency perturbations. *Journal of Advances in Modeling Earth Systems*, 13(5), e2021MS002461.

Iacobellis, S.F. and Somerville, R.C.J. (1991) Diagnostic modeling of the indian monsoon onset. Part i: model description and validation. *Journal of the Atmospheric Sciences*, 48(17), 1948–1959.

James, R.P. and Markowski, P.M. (2010) A numerical investigation of the effects of dry air aloft on deep convection. *Monthly Weather Review*, 138(1), 140–161.

Kealy, J.C., Efstathiou, G.A. and Beare, R.J. (2019) The onset of resolved boundary-layer turbulence at grey-zone resolutions. *Boundary-Layer Meteorology*, 171(1), 31–52.

Kuang, Z. (2008) Modeling the interaction between cumulus convection and linear gravity waves using a limited-domain cloud system–resolving model. *Journal of the Atmospheric Sciences*, 65(2), 576–591.

Kuang, Z. (2010) Linear response functions of a cumulus ensemble to temperature and moisture perturbations and implications for the dynamics of convectively coupled waves. *Journal of the Atmospheric Sciences*, 67(4), 941–962.

Kuang, Z. (2011) The wavelength dependence of the gross moist stability and the scale selection in the instability of column-integrated moist static energy. *Journal of the Atmospheric Sciences*, 68(1), 61–74.

Kuo, Y-H., Neelin, D., Chen, C.-C., Chen, W.-T., Donner, L.J., Gettelman, A., Jiang, X., Kuo, K.-T., Maloney, E. and Mechoso, C.R. (2020) Convective transition statistics over tropical oceans for climate model diagnostics: Gcm evaluation. *Journal of the Atmospheric Sciences*, 77(1), 379–403.

Lee, W.-H., Iacobellis, S.F. and Somerville, R.C.J. (1997) Cloud radiation forcings and feedbacks: general circulation model tests and observational validation. *Journal of Climate*, 10(10), 2479–2496.

Lin, J.-L., Lee, M.-I., Kim, D., Kang, I.-S. and Frierson, D.M.W. (2008) The impacts of convective parameterization and moisture triggering on agcm-simulated convectively coupled equatorial waves. *Journal of Climate*, 21(5), 883–909.

Liu, P., Satoh, M., Wang, B., Fudeyasu, H., Nasuno, T., Li, T., Miura, H., Taniguchi, H., Masunaga, H. and Xiouhua, F. (2009) An mjo simulated by the nicam at 14-and 7-km resolutions. *Monthly Weather Review*, 137(10), 3254–3268.

Lock, A.P., Brown, A.R., Bush, M.R., Martin, G.M. and Smith, R.N.B. (2000) A new boundary layer mixing scheme. Part i: scheme description and single-column model tests. *Monthly Weather Review*, 128(9), 3187–3199.

Lucas, C., Zipser, E.J. and Ferrier, B.S. (2000) Sensitivity of tropical west pacific oceanic squall lines to tropospheric wind and moisture profiles. *Journal of the Atmospheric Sciences*, 57(15), 2351–2373.

Mapes, B.E. (2004) Sensitivities of cumulus-ensemble rainfall in a cloud-resolving model with parameterized large-scale dynamics. *Journal of the Atmospheric Sciences*, 61(18), 2308–2317.

McCoy, D.T., Field, P.R., Schmidt, A., Grosvenor, D.P., Bender, F.A.-M., Shipway, B.J., Hill, A.A., Wilkinson, J.M. and Elsaesser, G.S. (2018) Aerosol midlatitude cyclone indirect effects in observations and high-resolution simulations. *Atmospheric Chemistry and Physics*, 18(8), 5821–5846.

Miltenberger, A.K., Field, P.R., Hill, A.A., Rosenberg, P., Shipway, B.J., Wilkinson, J.M., Scovell, R. and Blyth, A.M. (2018) Aerosol–cloud interactions in mixed-phase convective clouds–part 1: aerosol perturbations. *Atmospheric Chemistry and Physics*, 18(5), 3119–3145.

Muetzelfeldt, M.R., Plant, R.S., Clark, P.A., Stirling, A.J. and Woolnough, S.J. (2021) A climatology of tropical wind shear produced by clustering wind profiles from the met office unified model (ga7. 0). *Geoscientific Model Development*, 14(6), 4035–4049.

Muller, C.J. and Held, I.M. (2012) Detailed investigation of the self-aggregation of convection in cloud-resolving simulations. *Journal of the Atmospheric Sciences*, 69(8), 2551–2565.

Nie, J. and Sobel, A.H. (2016) Modeling the interaction between quasigeostrophic vertical motion and convection in a single column. *Journal of the Atmospheric Sciences*, 73(3), 1101–1117.

Randall, D.A., Kuan-Man, X., Somerville, R.J.C. and Iacobellis, S. (1996) Single-column models and cloud ensemble models as links between observations and climate models. *Journal of Climate*, 9(8), 1683–1697.

Randall, D.A., Wood, R.A., Bony, S., Colman, R., Fichefet, T., Fyfe, J., Kattsov, V., Pitman, A., Shukla, J. and Srinivasan, J. (2007) Climate models and their evaluation. In: *Climate Change 2007: The Physical Science Basis. Contribution of Working Group I to the Fourth Assessment Report of the IPCC (FAR)*. Cambridge University Press, pp. 589–662.

Raymond, D.J. (2007) Testing a cumulus parametrization with a cumulus ensemble model in weak-temperature-gradient mode. *Quarterly Journal of the Royal Meteorological Society: A Journal of the Atmospheric Sciences, Applied Meteorology and Physical Oceanography*, 133(626), 1073–1085.

Raymond, D.J. and Sessions, S.L. (2007) Evolution of convection during tropical cyclogenesis. *Geophysical Research Letters*, 34(6).

Raymond, D.J. and Zeng, X. (2005) Modelling tropical atmospheric convection in the context of the weak temperature gradient approximation. *Quarterly Journal of the Royal Meteorological Society: A Journal of the Atmospheric Sciences, Applied Meteorology and Physical Oceanography*, 131(608), 1301–1320.

Rio, C., Hourdin, F., Couvreux, F. and Jam, A. (2010) Resolved versus parametrized boundary-layer plumes. Part ii: continuous formulations of mixing rates for mass-flux schemes. *Boundary-Layer Meteorology*, 135(3), 469–483.

Rushley, S.S., Daehyun Kim, C.S., Bretherton and Ahn, M.-S. (2018) Reexamining the nonlinear moisture-precipitation relationship over the tropical oceans. *Geophysical Research Letters*, 45(2), 1133–1140.

Sessions, S.L., Herman, M.J. and Sentić, S. (2015) Convective response to changes in the thermodynamic environment in idealized weak temperature gradient simulations. *Journal of Advances in Modeling Earth Systems*, 7(2), 712–738.

Sessions, S.L., Sugaya, S., Raymond, D.J. and Sobel, A.H. (2010) Multiple equilibria in a cloud-resolving model using the weak temperature gradient approximation. *Journal of Geophysical Research: Atmospheres*, 115(D12).

Shipway, B.J. and Hill, A.A. (2012) Diagnosis of systematic differences between multiple parametrizations of warm rain microphysics using a kinematic framework. *Quarterly Journal of the Royal Meteorological Society*, 138(669), 2196–2211.

Siebesma, A.P. and Cuijpers, J.W.M. (1995) Evaluation of parametric assumptions for shallow cumulus convection. *Journal of Atmospheric Sciences*, 52(6), 650–666.

Sobel, A.H. and Bellon, G. (2009) The effect of imposed drying on parameterized deep convection. *Journal of the Atmospheric Sciences*, 66(7), 2085–2096.

Sobel, A.H., Bellon, G. and Bacmeister, J. (2007) Multiple equilibria in a single-column model of the tropical atmosphere. *Geophysical Research Letters*, 34(22).

Sobel, A.H. and Bretherton, C.S. (2000) Modeling tropical precipitation in a single column. *Journal of Climate*, 13(24), 4378–4392.

Stevens, R.G., Loewe, K., Dearden, C., Dimitrelos, A., Possner, A., Eirund, G.K., Raatikainen, T., Hill, A.A., Shipway, B.J. and Wilkinson, J. (2018) A model intercomparison of ccn-limited tenuous clouds in the high arctic. *Atmospheric Chemistry and Physics*, 18(15), 11041–11071.

Stratton, R.A. and Stirling, A.J. (2012) Improving the diurnal cycle of convection in gcms. *Quarterly Journal of the Royal Meteorological Society*, 138(666), 1121–1134.

Tompkins, A.M. (2000) The impact of dimensionality on long-term cloud-resolving model simulations. *Monthly Weather Review*, 128(5), 1521–1535.

Tulich, S.N. and Mapes, B.E. (2010) Transient environmental sensitivities of explicitly simulated tropical convection. *Journal of the Atmospheric Sciences*, 67(4), 923–940.

Walters, D., Baran, A.J., Boutle, I., Brooks, M., Earnshaw, P., Edwards, J., Furtado, K., Hill, P., Lock, A. and Manners, J. (2019) The met office unified model global atmosphere 7.0/7.1 and jules global land 7.0 configurations. *Geoscientific Model Development*, 12(5), 1909–1963.

Wang, S. and Sobel, A.H. (2011) Response of convection to relative sea surface temperature: cloud-resolving simulations in two and three dimensions. *Journal of Geophysical Research: Atmospheres*, 116(D11).
Wang, S. and Sobel, A.H. (2012) Impact of imposed drying on deep convection in a cloud-resolving model. *Journal of Geophysical Research: Atmospheres*, 117(D2).
Wang, S., Sobel, A.H. and Kuang, Z. (2013) Cloud-resolving simulation of toga-coare using parameterized large-scale dynamics. *Journal of Geophysical Research: Atmospheres*, 118(12), 6290–6301.
Wilson, D.R. and Ballard, S.P. (1999) A microphysically based precipitation scheme for the UK meteorological office unified model. *Quarterly Journal of the Royal Meteorological Society*, 125(557), 1607–1636.
Wilson, D.R., Bushell, A.C., Kerr-Munslow, A.M., Price, J.D. and Morcrette, C.J. (2008) Pc2: a prognostic cloud fraction and condensation scheme. i: scheme description. *Quarterly Journal of the Royal Meteorological Society: A Journal of the Atmospheric Sciences, Applied Meteorology and Physical Oceanography*, 134(637), 2093–2107.
Xu, K.-M. and Arakawa, A. (1992) Semiprognostic tests of the arakawa-schubert cumulus parameterization using simulated data. *Journal of the Atmospheric Sciences*, 49(24), 2421–2436.
Xu, K.-M. (1994) A statistical analysis of the dependency of closure assumptions in cumulus parameterization on the horizontal resolution. *Journal of the Atmospheric Sciences*, 51(24), 3674–3691.
Xu, K.-M., Cederwall, R.T., Donner, L.J., Grabowski, W.W., Guichard, F., Johnson, D.E., Khairoutdinov, M., Krueger, S.K., Petch, J.C. and Randall, D.A. (2002) An inter comparison of cloud-resolving models with the atmospheric radiation measurement summer 1997 intensive observation period data. *Quarterly Journal of the Royal Meteorological Society: A Journal of the Atmospheric Sciences, Applied Meteorology and Physical Oceanography*, 128(580), 593–624.
Xu, K.-M., Zhang, M., Eitzen, Z.A., Ghan, S.J., Klein, S.A., Wu, X., Xie, S., Branson, M., Del Genio, A.D., Iacobellis, S.F., Khairoutdinov, M., Lin, W., Lohmann, U., Randall, D.A., Somerville, R.C.J., Sud, Y.C., Walker, G.K., Wolf, A., John, J., Yio, J. and Zhang, J. (2005) Modeling springtime shallow frontal clouds with cloud-resolving and single-column models. *Journal of Geophysical Research: Atmospheres*, 110(D15).
Xie, S., Xu, K.-M., Cederwall, R.T., Bechtold, P., Del Genio, A.D., Klein, S.A., Cripe, D.G., Ghan, S.J., Gregory, D., Iacobellis, S.F., Krueger, S.K., Lohmann, U., Petch, J.C., Randall, D.A., Rotstayn, L.D., Somerville, R.C.J., Sud, Y.C., Von Salzen, K., Walker, G.K., Wolf, A.B., John Yio, J., Guang, Z. and Zhang, M. (2002) Intercomparison and evaluation of cumulus parametrizations under summertime midlatitude continental conditions. *Quarterly Journal of the Royal Meteorological Society: A Journal of the Atmospheric Sciences, Applied Meteorology and Physical Oceanography*, 128(582), 1095–1135.

How to cite this article: Daleu, C.L., Plant, R.S., Stirling, A.J. & Whitall, M. (2023) Evaluating the CoMorph-A parametrization using idealized simulations of the two-way coupling between convection and large-scale dynamics. *Quarterly Journal of the Royal Meteorological Society*, 1–23. Available from: https://doi.org/10.1002/qj.4547

APPENDIX A

SUMMARY OF COMORPH-A AND ITS ENTRAINMENT FORMULATION

CoMorph-A is the new diagnostic mass flux convection parametrization under development at the Met Office (Whitall *et al*, in preparation). It represents unresolved vertical transport of momentum, heat, moisture, and other scalars by rearranging mass (and its associated properties) within each model column, such that buoyant air is transported upwards. Convective updraughts and downdraughts are represented by diagnostic vertical budget equations for the mass flux and the properties of the vertically-transported air. However, in CoMorph-A, the traditional mass flux framework is generalized and extended.

- Traditionally, updraughts are prescribed to start from a predetermined cloud-base height, which is treated as a lower boundary condition for the vertical integrals, and requiring a closure assumption for the initial mass flux at this height. In CoMorph-A, mass flux may initiate simultaneously and independently from all heights in the column where local vertical instability exists. There is no closure for the cloud-base mass flux, which is an emergent property of the scheme, dependent on the proportion of the sub-cloud-layer mass flux that detrains before reaching saturation. The mass flux profile M ($\mathrm{kg \cdot m^{-2} \cdot s^{-1}}$) follows

$$\frac{\partial M}{\partial z} = E - D + G, \tag{A.1}$$

  where the terms on the right-hand side represent entrainment E, detrainment D, and convective initiation G. The traditional approach is retrieved by omitting the initiation term G and prescribing an ad-hoc lower boundary condition at cloud base (or equivalently by defining G to be a delta function that is non-zero only at the predefined cloud-base height). The rate of initiation G is parametrized as a function of the local static instability at each height,

$$G = \rho\sqrt{-N^2} \tag{A.2}$$

  (where N^2 [$\mathrm{s^{-2}}$] is the dry-static stability in cloud-free air or moist-static stability in cloudy air (G is set to zero at levels where N^2 is positive). This formulation allows CoMorph-A to respond naturally to instability at any height.
- The detrainment rate D is based on an assumed probability density function (PDF) of in-plume buoyancy and other properties. For each convective draught, we

vertically integrate not only the mean properties of the plume, but also separate "core" properties that represent the least-dilute elements within the bulk plume – compare with the "core-cloak" model proposed by Gu et al. (2020). The parcel core is integrated using a lower entrainment rate than the parcel mean, so that it typically has a higher buoyancy than the parcel mean. Each transported quantity is assumed to follow a power-law PDF within the plume, extending out from its core value (with the power constrained by the ratio of core buoyancy over mean buoyancy). At each height, the PDFs are partitioned into non-detrained air (the portion of the PDF that remains buoyant) and detrained air (the portion that has become negatively buoyant). The ascent terminates whenever the parcel core is negatively buoyant, implying that the whole PDF represents detrained air.

The detrainment calculation uses an implicit numerical method; that is, the environment virtual temperature used to find the position in the assumed PDF where buoyancy is zero as a pre-estimate of the value after the convection increments are added on. This ensures that the scheme cannot "overstabilize", that is, create an environment that is too warm for the parcel to have been able to rise through it. Avoiding numerical overshoot in this way allows the mass flux to evolve smoothly over successive time steps.

- The entrainment rate E is assumed to be inversely proportional to a "parcel radius" R, which quantifies the horizontal length-scale of the convective updraughts:

$$E = M\frac{0.2}{R}. \tag{A.3}$$

The parcel radius R is assumed to scale with the length scale of the turbulence in the layer where the convection triggers – (see Stratton and Stirling, 2012, who set the entrainment rate inversely proportional to mixed-layer depth). In CoMorph-A, the parcel initial R_{init} at each height is parametrized as

$$R_{\text{init}} = 8\alpha\frac{K_{\text{m}}}{\sqrt{\overline{w'^2}}}, \tag{A.4}$$

where K_{m} ($\text{m}^2\cdot\text{s}^{-1}$) is the turbulent diffusivity and $\overline{w'^2}$ ($\text{m}^2\cdot\text{s}^{-2}$) is the turbulent vertical velocity variance; both are outputs from the boundary-layer scheme. This gives a turbulence length-scale that naturally accounts for both the local and non-local turbulence parametrized by the boundary-layer scheme. Within the surface layer of a well-mixed boundary layer it scales with the boundary-layer depth z_h. Note that the factor of 8 gives a length scale equal to $z_h/2$ in the middle of the mixed layer.

The preceding dimensionless scaling factor α is optionally set as a linear function of the grid-mean surface precipitation rate Pr from the previous time step to allow the scheme to crudely represent increased organization of the convection by precipitation-driven cold pools, which promote larger scale updraughts with lower entrainment rates:

$$\alpha = \alpha_0 + MIN\left(\frac{\text{Pr}}{\text{Pr}_{\text{max}}}\frac{q_{\text{ref}}}{q_{\text{v}}}, 1\right)(\alpha_{\text{max}} - \alpha_0), \tag{A.5}$$

where q_{v} is the vertical-mean water vapour content of the surface layer of the well-mixed boundary layer. We fixed the values of $\text{Pr}_{\text{max}} = 0.00035\,\text{kg}\cdot\text{m}^{-2}\cdot\text{s}^{-1}$, $q_{\text{ref}} = 0.02\,\text{kg}\cdot\text{kg}^{-1}$, $\alpha_0 = 0.45$, and $\alpha_{\text{max}} = 2.0$. This linear ramp function allows CoMorph-A to smoothly transition from simulating non-precipitating shallow cumulus with small size (high entrainment rates) through to heavily precipitating deep convection with large size (low entrainment rates), for a given turbulence length-scale in the triggering layers. This unified approach removes any need to have separate schemes for "shallow", "deep", or "congestus" convection; all are simulated with the same code by adaptively varying the parcel radius R.

- In CoMorph, convective updraught mass may initiate independently from each height, according to Equation (A.2). Equations A.4 and A.5 give the radius of the mass source initiating from each height, but these radii must be vertically averaged to obtain the net radius R of the combined parcel as it rises. The parcel radius evolves with height following

$$\frac{\partial R}{\partial z} = \frac{G}{M}(R_{\text{init}} - R) + R\frac{\frac{\partial}{\partial z}[(M/\rho)^{1/3}]}{(M/\rho)^{1/3}}. \tag{A.6}$$

The first term on the right-hand side performs mass-flux-weighted averaging of the radii of parcels initiating at different heights. The second term accounts for change in the volume of an assumed spherical thermal with height, due to change in the thermal's mass and decrease in air density. In the current version, the term $(\partial/\partial z)[(M/\rho)^{1/3}]$ is evaluated using only the change in mass-flux due to entrainment E; the initiating mass-source G and detrainment D are excluded from the volume change. This is because G and D are thought to selectively add or remove thermals from a population, instead of uniformly changing the mass of every thermal.

- CoMorph-A includes an intermediate-complexity interactive microphysics parametrization to predict the formation of liquid cloud, rain, ice cloud, and graupel within the parcel. The rate at which each

hydrometeor type falls out of the parcel into the environment is modelled based on its fall speed. Traditional mass-flux convection schemes adjust the parcel to saturation at each height and do this with respect to ice saturation when the parcel temperature falls below freezing. CoMorph's in-parcel microphysics scheme allows the parcel and detrained air to remain supersaturated with respect to ice, with a gradual glaciation of the in-parcel water content with height, as is observed.

- CoMorph-A does not itself produce convective precipitation at the surface. Instead, rain, ice, and graupel that fall out of the parcel or are contained in the detrained air are added to the model's prognostic fields for the masses of these quantities. The large-scale microphysics scheme then simulates the fall of the convectively generated precipitation to the surface, along with its evaporation, melting, accretion of large-scale cloud, and so forth. To aid coupling to the large-scale microphysics scheme at coarse resolution, both it and CoMorph-A use a prognostic field for the subgrid fraction of rain and graupel. CoMorph-A sets this to a suitably small value where fractionally small convection is the main source of precipitation mass.